Review Article

Nano Research
2022, 15(10): 9614–9630

ISSN 1998-0124 CN 11-5974/O4
https://doi.org/10.1007/s12274-022-4817-1

Hydrogel-based composites beyond the porous architectures for electromagnetic interference shielding

Yunfei Yang[1,§], Mingrui Han[1,§], Wei Liu[2,3], Na Wu[4] (✉), and Jiurong Liu[1] (✉)

[1] *Key Laboratory for Liquid-Solid Structural Evolution and Processing of Materials, School of Materials Science and Engineering, Shandong University, Jinan 250061, China*
[2] *State Key Laboratory of Crystal Materials, Shandong University, Jinan 250100, China*
[3] *Shenzhen research institute of Shandong University, Shenzhen 518052, China*
[4] *Department of Chemistry and Applied Biosciences, ETH Zurich, Zurich CH-8093, Switzerland*
[§] *Yunfei Yang and Mingrui Han contributed equally to this work.*

Received: 21 June 2022 / **Revised:** 19 July 2022 / **Accepted:** 24 July 2022

ABSTRACT

With the rapid development of the electronic industry and wireless communication technology, electromagnetic interference (EMI) or pollution has been increasingly serious. This not only severely endangers the normal operation of electronic equipment but also threatens human health. Therefore, it is urgent to develop high-performance EMI shielding materials. The advent of hydrogel-based materials has given EMI shields a novel option. Hydrogels combined with conductive functional materials have good mechanical flexibility, fatigue durability, and even high stretchability, which are beneficial for a wide range of applications, especially in EMI shielding and some flexible functional devices. Herein, the current progress of hydrogel-based EMI shields was reviewed, in the meanwhile, some novel studies about pore structure design that we believe will help advance the development of hydrogel-based EMI shielding materials were also included. In the outlook, we suggested some promising development directions for the hydrogel-based EMI shields, by which we hope to provide a reference for designing hydrogels with excellent EMI shielding performance and multifunctionalities.

KEYWORDS

electromagnetic interference (EMI) shielding, porous, hydrogels, structural design, composites

1 Introduction

With the rapid progress in electronic equipment and wireless technology, the booming issues of electromagnetic interference (EMI) or pollution have brought about harm to electric devices and human health [1–5]. Therefore, employing EMI shielding materials to protect the normal operation of electronic devices and human beings from electromagnetic radiation is essential [6, 7]. Although bulk materials like traditional metal-based EMI shields are utilized widely, the easy corrosion, high density, poor processability, and mechanical flexibility hinder their further application, especially in the burgeoning fields such as flexible bioelectronic devices and the Internet of Things (IoT) [8–11]. Exploring the advanced EMI shielding materials with high mechanical flexibility, easy processability, as well as high and controllable EMI shielding effectiveness (SE) is necessary for promoting the development of novel and multifunctional devices.

Recently, thanks to the high conductivity, low mass density, and decent flexibility, great efforts have been invested in the polymeric shielding composites embedded with functional nanomaterials such as carbon nanotubes (CNTs) [12, 13], reduced graphene oxide (rGO) [14, 15], transition metal carbides and/or nitrides (MXenes) [16–20], and silver nanowires (AgNWs) [21, 22]. Particularly, the introduction of the porous structure to generate abundant interior surfaces/interfaces in the shielding composites is an efficient strategy to improve the multiple reflections of incident electromagnetic waves (EMWs), further enhancing the EMI shielding performance [23–28]. As a class of porous engineering materials, hydrogels, composed of a network of cross-linked hydrophilic building blocks surrounded by water, not only maintain the porous structure but also possess a water-enriched interior environment [29, 30]. On the one hand, most of the functional nanomaterials can be easily and uniformly dispersed in the hydrogels to form the conductive paths, contributing to the high conductive loss of incident EMWs [31, 32]. On the other hand, the water can generate potent polarization loss to consume the EMWs energy due to the change of hydrogen-bond networks as well as the polarization of water molecules in gigahertz (GHz) and terahertz (THz) band [33–35]. Combined with the efficient multiple reflection capability derived from the existed porous structure, the hydrogels show great potential for novel and high-performance EMI shielding materials. In addition, the mechanical ultra-flexibility and stretchability of hydrogels are the unique superiority that traditional porous materials like foams and aerogels hardly possess. However, to the best of our knowledge, the review work about the hydrogel-based EMI shielding materials has been rarely reported.

Here, we summarized the recent research on the hydrogel-based materials for EMI shielding applications, focusing on the

Address correspondence to Na Wu, na.wu@org.chem.ethz.ch; Jiurong Liu, jrliu@sdu.edu.cn

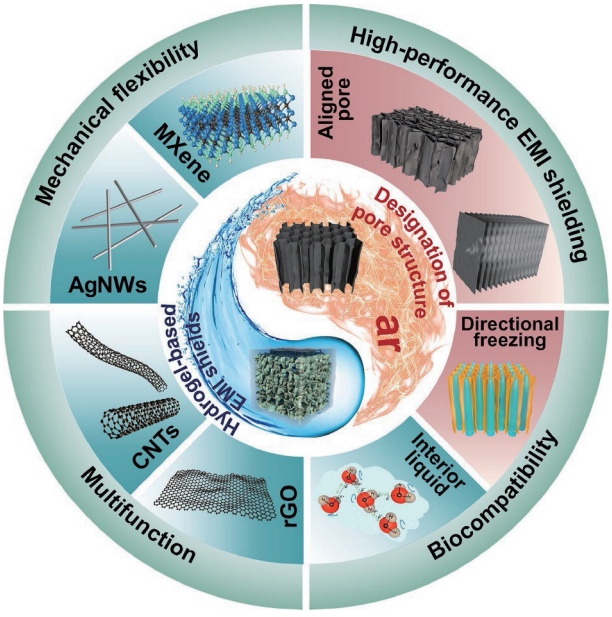

Figure 1 Schematic illustration of hydrogel-based EMI shields beyond the porous architectures.

preparation, current status, and ongoing challenges as well as outlook (Fig. 1). Considering the composition and structural characteristics of hydrogels, the hydrogel-based composite EMI shields were categorized as hydrogels embedded with various inorganic conductive nanomaterials, hydrogels integrated with conductive polymers, and the hydrogels showing multifunctionalities. Furthermore, we noticed that the design of the porous structure is vital for achieving high-performance and controllable EMI shields. Compared with the randomly porous structures, biomimetic ordered pores like honeycomb and lamellar aligned pores can improve the multiple reflections of incident EMWs, enhancing the interactions between EMWs and cell walls and thus the EMI shielding performance [36–40]. Although this has been reported in the porous foam/aerogel-based EMI shields, the EMI shielding hydrogels with biomimetic ordered pores have not been developed yet. Therefore, to promote the development of the hydrogel-based EMI shields, we have also concluded some typical porous foam/aerogel-based EMI shields with biomimetic ordered porous structures. We hope this review can advance the investigation of the relationships between the controllable interior pore structure and EMI shielding performance for preparing more high-performance porous shields including but not limited to the hydrogel-based EMI shields.

2 Hydrogel-based materials for high-performance EMI shielding

Profiting from the water-rich nature and the soft polymer-based building blocks, the broad application of hydrogels includes, but is not limited to, tissue engineering, soft electronics, and EMI shielding. As the water is made of polar molecules, the polarization of H_2O molecules and variations of hydrogen-bond networks can be evoked under the applied electromagnetic field [41–43]. This guarantees the capability of water on attenuating penetrated EMWs [35, 44]. Thus, the hydrogels with aqueous environments as EMI shields are promising. Moreover, due to the soft cross-linked polymer-based building blocks, the excellent mechanical properties of hydrogels, including ultra-flexibility, elasticity, fatigue resistance, and especially stretchability, are expected to overcome the poor mechanical toughness of three-dimensional (3D) foam/aerogel. In short, the potent absorption loss capability and remarkable mechanical toughness promise the hydrogels as high-performance EMI shields.

2.1 Preparation of hydrogel-based EMI shields

The network of crosslinked polymer chains is essential for constructing the hydrogels with a stable 3D structure. By forming the dynamic ionic/hydrogen bonds between polymers or creating covalently crosslinked networks, the polymer chains dispersed in aqueous solution are assembled to construct the hydrogels with outstanding elasticity and flexibility [45–47]. Despite the interactions between inorganic nanoparticles are weak, the crosslinked polymer networks can guarantee that the conductive fillers can be embedded into the polymer matrix to prepare the freestanding and conductive hydrogels [48–50]. The preparation methods of hydrogel-based EMI shields mainly include the physical crosslinking methods like crystallization crosslinking and coordination interactions, and chemical crosslinking.

2.1.1 Hydrogel fabrication by physical crosslinking

The increased crystallinity of polymer can act as physically crosslinking sites in the network, resulting in the formation of hydrogels [51, 52]. In the freeze-thawing treatment, when the bulk solvents or low molecular solutes crystallize upon freezing, the reduced polymer chain space and increased polymer concentration force the polymer chain to align and associate with the joining network structure of a hydrogel via hydrogen bonds and crystallinity. According to the work reported by Hao et al. [53], after embedding the Fe_3O_4 clusters into poly(3,4-ethylenedioxythiophene):poly(styrene sulfonic acid) (PEDOT:PSS) and polyvinyl alcohol (PVA) aqueous solutions, the hydrogels were constructed for EMI shielding through the freeze-thawing method as schematically illustrated in Figs. 2(a)–2(c). In the preparation process, the exposure of solutions to low temperature causes water molecules to freeze, expelling polymer chains and forming regions of high polymers concentration. Here, the polymer chains of PVA and PEDOT:PSS come into close contact with each other and facilitate hydrogen bonding as well as crystallization, forming the hydrogels. This endowed the hydrogels with decent mechanical properties with the stretchability of 900% strain that aerogels/foams hardly matched (Fig. 2(d)). The conductive PEDOT:PSS formed a continuous and uniform conductive path, and had high electrical conductivity to improve the reflection efficiency of incident EMWs. In addition, introducing the Fe_3O_4 also lifted the complex permeability and permittivity, further increasing the EMI SE (Fig. 2(e)). To this end, the Fe_3O_4/PEDOT:PSS/PVA hydrogels exhibited more than 46 dB in the X band (8.2–12.4 GHz). Although the freeze-thawing crosslinking is easy to operate, the cycle should be carried out several times (3 to 9 times) to ensure the crystallinity of polymers for creating strong and stable hydrogels, taking up to several days. The shrinkage and water loss inevitably impair the porous structure and water-rich environment in the process, limiting the absorption capability of hydrogel-based EMI shields.

In comparison, the ionic/electrostatic crosslinking of metal ions with simple and mild procedures possesses an immediate gelation process [54]. Utilizing the interactions between metal ions and functional groups, Lai et al. assembled a hydrogel of reduced graphene oxide (rGO)/poly(acrylic acid) (PAA)/chitosan (CS) chains/amorphous calcium carbonate (ACC) for EMI shielding [55]. Firstly, the PAA polymer chains were initially cross-linked by the chelation interactions between $COOH^-$ of PAA and Ca^{2+}. With the addition of CO_3^{2-}, ACC nanoparticles were further formed to physically cross-link the PAA chains. Meanwhile, the hydrogen bonds were also formed between polar groups of PAA, CS, and rGO nanosheets (Figs. 2(f) and 2(g)). Benefiting from the strong polarity of freely movable H_2O molecules, ionic conduction of Ca^{2+}

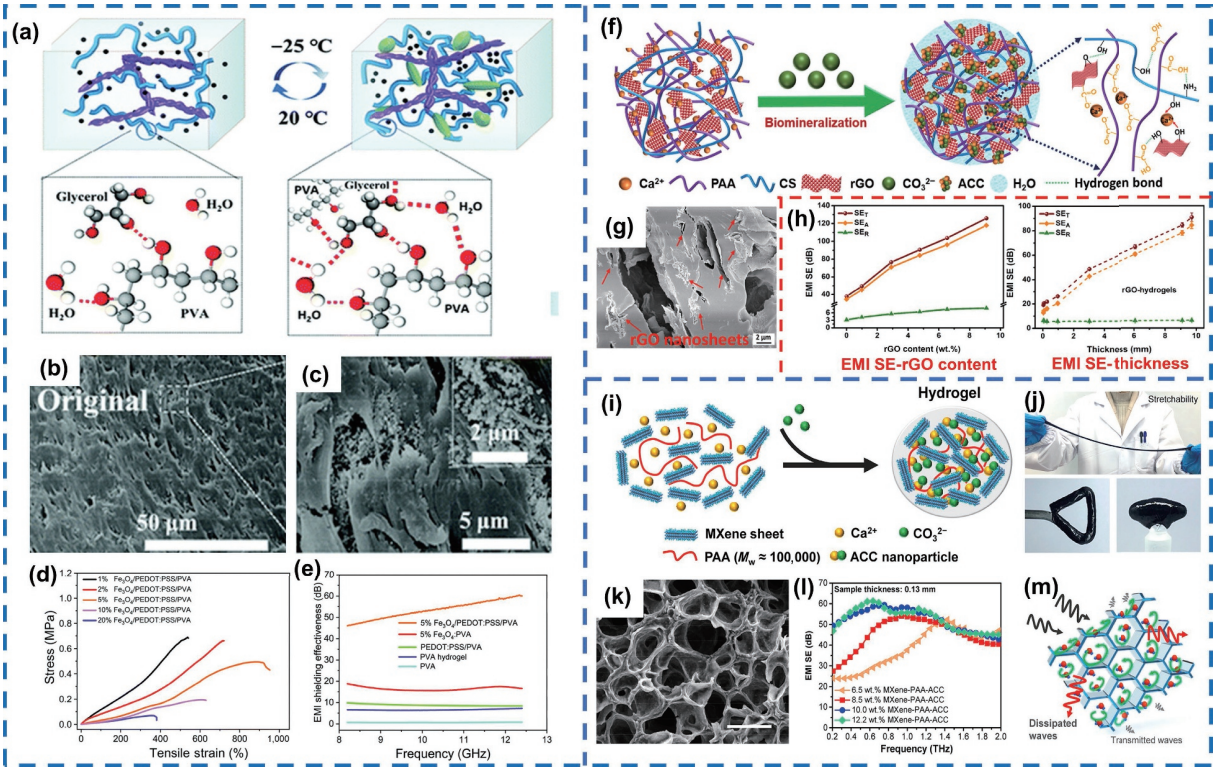

Figure 2 (a) Schematic of the fabrication of Fe_3O_4/PEDOT:PSS/PVA hydrogels through freeze-thawing, (b) and (c) scanning electron microscopy (SEM) images, (d) mechanical properties, and (e) EMI SE of Fe_3O_4/PEDOT:PSS/PVA hydrogels. Reproduced with permission from Ref. [53], © The Royal Society of Chemistry 2021. (f) Schematic of the fabrication for rGO/PAA/CS/ACC hydrogels by metal ions coordination, (g) SEM image, and (h) EMI SE of rGO/PAA/CS/ACC hydrogels. Reproduced with permission from Ref. [55], © Elsevier Ltd. 2021. (i) Schematic of the fabrication for MXene/PAA/ACC hydrogels, (j) stretchability, flexibility, and (k) SEM images of hydrogel, and (l) and (m) EMI SE and shielding mechanism of rGO-based hydrogels. Reproduced with permission from Ref. [57], © American Chemical Society 2021.

and PAA^-, and highly conductive rGO nanosheets, the rGO (4.76 wt.%)/PAA/CS/ACC hydrogels obtained the EMI SE of 20 to 90 dB at a thickness of 0.04 to 9.46 mm, respectively (Fig. 2(h)). Notably, the authors also tried to fabricate the hydrogels without CS but only obtained the liquid-like PAA/ACC gel. This was because the plentiful hydroxyl and amino groups of CS contributed to the abundant hydrogen bonds connecting between PAA, rGO, and CS, and the correspondingly increased crosslinking density promoted the synthesis of the hydrogels. Nevertheless, a high fraction of polymers is unfavorable for fully utilizing the conductive fillers and limiting the conductivity of hydrogels. Fortunately, besides the crosslinking between polymers, some conductive nanomaterials with a negative charge, such as MXene nanosheets [56], could interact with metal ions to strengthen the mechanical property of hydrogels via increasing crosslinking density. To this end, Zhu et al. prepared the hydrogel-based EMI shields incorporated with MXene and PAA/ACC (Fig. 2(i)) [57]. The addition of ACC not only promoted the chelation between PAA chains but also contributed to the ionic bonds between MXene sheets and Ca^{2+}. From this, without extra addition of polymers, the MXene-based PAA/ACC hydrogels with porous structure possessed decent mechanical properties involving ultra-flexibility and stretchability (Figs. 2(j) and 2(k)). Simultaneously, the crosslinked MXene nanosheets contributed to the formation of conductive networks and brought moderate conductivity to hydrogels. Correspondingly, in Fig. 2(l), the MXene/PAA/ACC hydrogels showed the EMI SE of 45.3 dB at a low thickness of 0.13 mm in the THz band (0.2–2.0 THz).

To sum up, the physical crosslinking is mainly derived from the dynamic hydrogen bond and Coulomb interactions between polar groups and metal ions, while these can be destabilized by variations in pH, ionic strength, or temperature.

2.1.2 *Hydrogel fabrication by chemical crosslinking*

Compared with physical methods, the chemical crosslinking is better at stabilizing a hydrogel matrix because the covalent bonds are created by the chemical reactions of functionalized polymers or monomers with crosslinking agents, ensuring the hardly soluble character of the hydrogels [41].

Utilizing the epichlorohydrin (EPI) as the crosslinker, Bai et al. fabricated the stretchable and compressible cellulose/MXene hydrogels for EMI shielding (Figs. 3(a)–3(e)) [58]. In the alkaline condition, the alcoholate anion derived from hydroxyl groups of cellulose attacked the epoxy groups of EPI to form a monoester of chloropropanediol. Then, the new epoxy groups yielded by chloride displacement rearranged the chloropropanediol monoester and then reacted with the hydroxyl groups of another cellulose, crosslinking the EPI and cellulose to form the hydrogels (Fig. 3(b)) [58]. In addition, the cellulose contributed to the uniform dispersion of MXene to build an efficient conductive network in alkaline conditions. Integrating the high conductivity of MXene, porous structure in hydrogels, and polarization loss from water and polar groups, this hydrogel exhibited the absorption-dominant EMI SE of 30 dB in the X-band (Figs. 3(f) and 3(g)). Nevertheless, during the crosslinking process, the cross-link agents might have some side reactions, for example, some EPI molecules might only react with one hydroxyl group of cellulose and some unreacted EPI hydrolyzes to glycerol. This caused loose crosslinking networks, and the mechanical property of cellulose/MXene hydrogel was less than fantastic, exhibiting the modulus of merely 9.46 kPa (Fig. 3(h)). Thus, the stability of interaction bonds and the amount of crosslinking density are both vital for hydrogel-based EMI shields in practical applications. Wu et al. utilized glutaraldehyde as the chemical crosslinking agent to prepare the MXene/chitosan hydrogels. The aldehyde group on

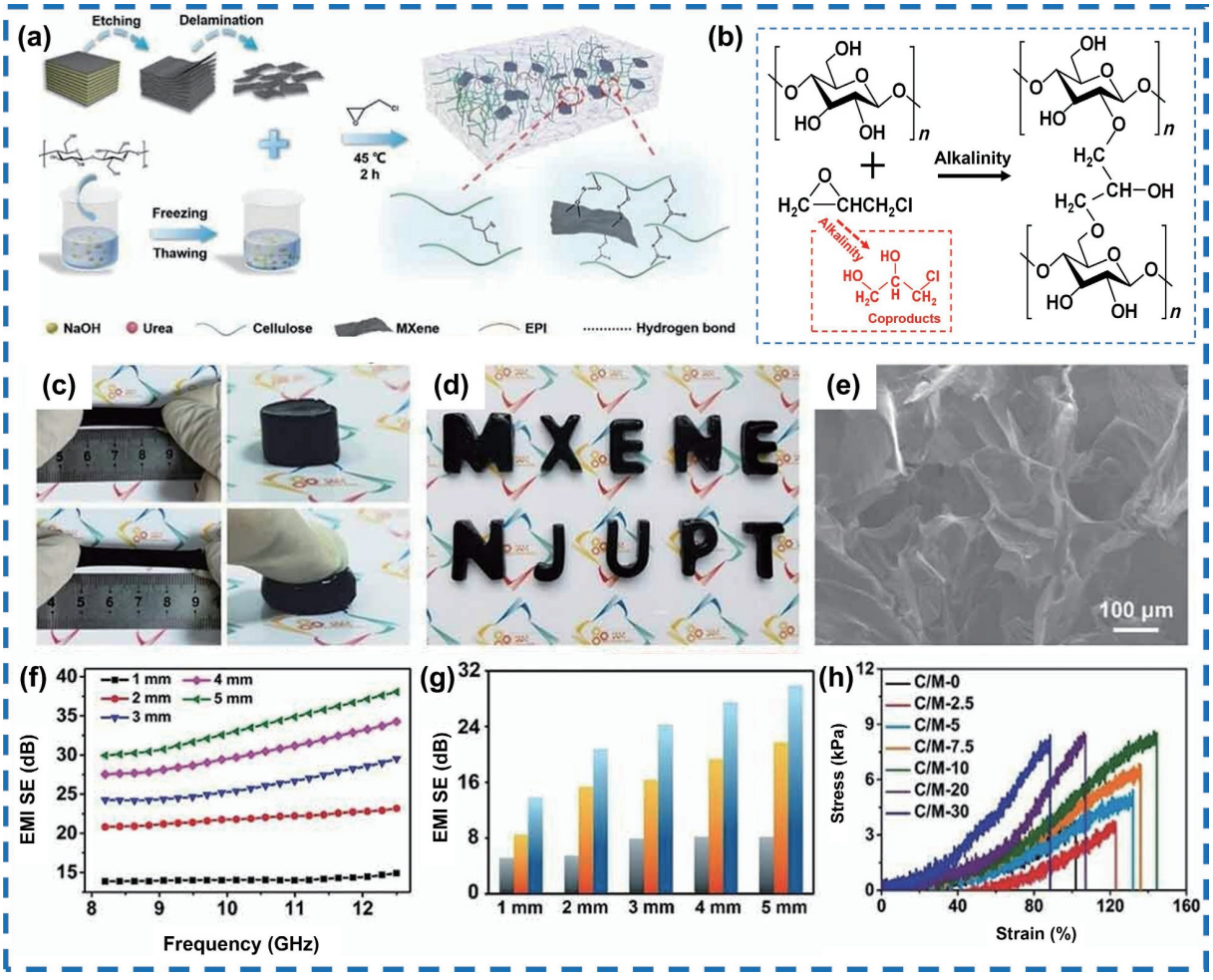

Figure 3 (a) Schematic of fabrication MXene/cellulose hydrogel and (b) the mechanism of chemical crosslinking between cellulose and EPI. (c) and (d) flexibility of hydrogels, (e) SEM images of hydrogel, (f) and (g) EMI SE, and (h) the stress–strain curves. Reproduced with permission from Ref. [58], © Taylor & Francis Group, LLC 2022.

glutaraldehyde molecules could react with the primary amino groups of chitosan chains to form the imine bonds between polymer chains, constructing the macrostructure with adequate strength. And the MXene/chitosan hydrogels derived aerogels exhibited the excellent EMI SE of ~ 61.4 dB in the X band [60]. Zhao et al. fabricated the Co(II) doped sodium alginate/melamine hydrogels, and the acylation reaction, where a portion of nitrogen was probably acylated by a few carboxyls, further enhanced the crosslinking degree. These hydrogel-derived carbonaceous materials also revealed a decent EMI protection performance [61].

From the above discussions, we can conclude that the single crosslinking treatment for constructing hydrogels-based EMI shields usually has inevitable defects, limiting the practical applications. In the context of effective EMI shielding capability, controlling the wide range of mechanical properties can expand the application scenario of hydrogels. Recently, various sophisticated strategies have been introduced in synthetic hydrogels such as double network hydrogels, sliding-ring hydrogels, and dual crosslinked hydrogels [62]. These hydrogels with multiple intertwined crosslinked networks balance the mechanical performance by combining high strength and toughness, which makes them become the research hotspots. Thus, this can be the following development direction of constructing hydrogel-based EMI shields.

2.2 Research progress of hydrogel-based EMI shields

Generally, the high conductivity of the material is an essential role in achieving high-performance EMI shields. Nevertheless, the polymer-based building blocks of hydrogels, such as PVA [63], polyacrylamide (PAAM or PAM) [64], and cellulose [65], are typically non-conductive, leading to insufficient EMI shielding capability. The factors affecting the shielding performance of hydrogels contain conductivity, multiple reflections of incident EMWs, and conductive and polarization loss capabilities. Therefore, filling conductive nanomaterials to achieve considerable conductivity is the key point for developing hydrogel-based EMI shielding materials. Meanwhile, retaining the internal water-rich environment is also forward to the potent polarization loss capability derived from the changed hydrogen-bond networks and molecules polarization under the EM fields. Probing the effects of the components in hydrogels on EMI shielding performance is warranted. Thus, this discussion can be divided into three main categories according to the components and functionalities, including the hydrogel-based EMI shields embedded with the inorganic conductive fillers, the hydrogel-based EMI shields integrated with the conductive polymers, as well as hydrogel-based EMI shields showing multifunctionalities.

2.2.1 Hydrogel-based EMI shields embedded with various inorganic conductive nanomaterials

Recently, thanks to the large aspect ratio and high conductivity, the one-dimensional (1D) nanomaterials such as silver nanowires (AgNWs) [21, 66] and CNTs [12, 37] are most popularly employed for constructing 3D conductive networks and improving the conductivity and EMI shielding performance of hydrogels. Through vacuum-assisted filtration, the AgNWs were

attached to the PVA/aramid nanofibers (ANFs) mats fabricated by electrospinning. Furthermore, Zhou et al. fabricated the sandwich-structured hydrogels combined with the ANF-reinforced PVA hydrogels layer and AgNWs/PVA layer (Figs. 4(a)–4(c)) [67]. The crystalline structure of PVA formed during electrospinning acts as physical crosslinking sites to form a 3D network with ANFs, and then the hydrogels were constructed by swelling in the water. In addition, the ANFs further reinforced the mechanical properties of hybrid hydrogels, exhibiting the modulus of 10.7–15.4 MPa, which were superior to those of pure PVA hydrogel (Fig. 4(d)). With the addition of AgNWs increasing from 0.02 vol.% to 0.23 vol.%, the conductivity of hybrid hydrogels reached 16,000 S·m^{-1}, and the EMI SE in X-band enhanced from 32 to 52 dB at the thickness of approximately 0.3 mm (Figs. 4(e) and 4(f)). To clarify the contribution mechanism of AgNWs to the overall SE of the conductive hydrogels, the SE_A and SE_R were exhibited in Fig. 4(f). It was noticed that the enhancement of more than 20 dB mainly originated from SE_A as the SE_R increased slightly. The addition of highly conductive AgNWs mainly contributed to the formation of the AgNWs layer with potent conductive loss capability, lengthening the propagation path of incident EMWs and thus dissipating the EMWs more. This mainly promoted the absorption loss dominated EMI SE. Considering the high density, the metal-based fillers were expected to be replaced by lightweight, highly conductive, and chemically stable carbon-based 1D conductive nanomaterials, such as CNTs [32, 40]. More importantly, the CNTs with huge aspect ratios are much more able to form the conductive networks, increasing the conductivity of hydrogels. Yang et al. fabricated the hydrogels by incorporating multiwalled CNTs (MWCNTs) into hydrophobically associated PAM hydrogels by using cellulose nanofiber (CNF) as the dispersant (Fig. 4(g)) [68]. The admirable dispersion of MWCNTs

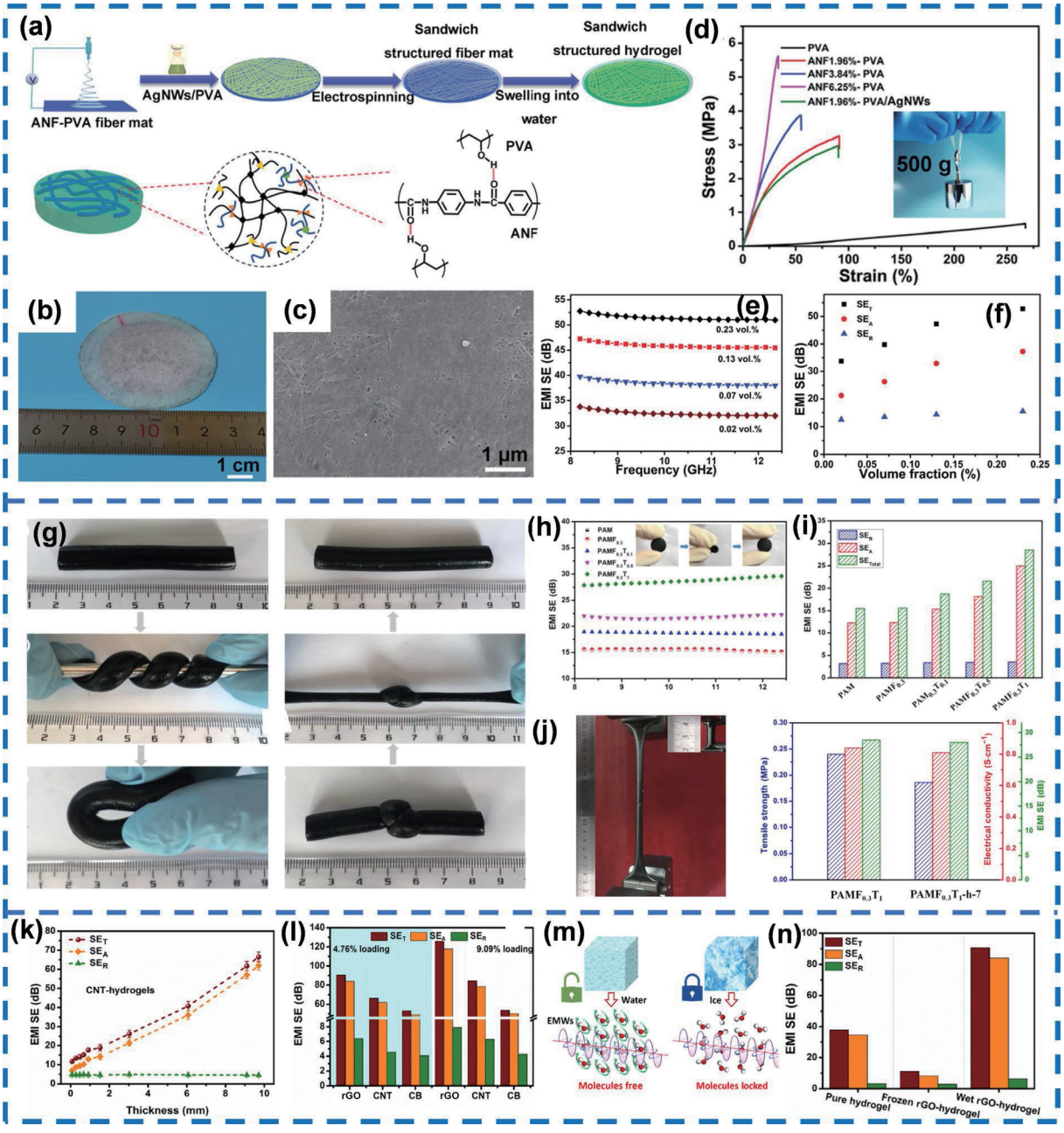

Figure 4 (a) Schematic of fabrication AgNWs/PVA hydrogel, (b) the morphology and (c) SEM image of hydrogel, (d) stress–strain curves, and (e) and (f) EMI SE of AgNWs/PVA hydrogels. Reproduced with permission from Ref. [67], © Wiley-VCH GmbH 2021. (g) The photograph of flexible MWCNTs/PAM/CNF hydrogel. (h) and (i) EMI SE of hydrogels with different filler content, and (j) self-healing property of hydrogels. Reproduced with permission from Ref. [68], © American Chemical Society 2018. (k) EMI SE of CNTs-based hydrogels, (l) comparison of CNTs- and rGO-based hydrogel on EMI SE, (m) schematic illustrations of EMWs transfer across water and ice, and (n) EMI SE of frozen and wet rGO-based hydrogels. Reproduced with permission from Ref. [55], © Elsevier Ltd. 2021.

also facilitates the close interconnection between MWCNTs to form a strong and well-established conductive network throughout the hydrogels. As the result, with the increased MWCNT content from 0.1 wt.% to 1 wt.%, the electrical conductivities of these as-prepared hydrogels gradually enhanced to 0.85 $S \cdot m^{-1}$, and the EMI SE increased from 15 to 28.5 dB at a thickness of 2 mm (Figs. 4(h) and 4(i)). The enhancement of EMI SE was mainly ascribed to the SE_A derived from the increased charge carriers with greater dissipation capacity with increased MWCNT contents. Notably, benefiting from the reversible crosslink bonds such as dynamic hydrogen bonding and ionic interactions, this conductive hydrogel also possessed the autonomously self-healing capability. After self-healed from two sections of hydrogel contacting for a week, the mechanical, electrical, and EMI shielding properties remained invariable, which cannot be achieved by bulk and foam/aerogel-based EMI shields (Fig. 4(j)). Lai et al. also reported the self-healing PAA/CS/ACC hydrogel embedded with CNTs [55]. As the weight mass of CNTs was 4.76 wt.%, the EMI SE in X-band was 11 to 60 dB at a thickness of 0.07 to 9.46 mm, respectively (Fig. 4(k)). Nevertheless, in Fig. 4(l), the EMI SE of CNT-based hydrogels was still below that of rGO-based hydrogels (20–90 dB, 0.04–9.46 mm) with the same weight mass of functional nanomaterials. On the one hand, due to the two-dimensional (2D) structure, compared with 1D CNTs, the connected rGO nanosheets provided more interfacial areas in the cell walls to facilitate the multiple reflections of incident EMWs. This could be proven by the higher SE_A of rGO-based hydrogels (84.22 dB) than that of CNT-based hydrogels (61.95 dB). On the other hand, the lower contact resistance between rGO nanosheets contributed to 3D networks with higher conductivity, contributing to the higher capability of rGO-based hydrogels to attenuate EMWs. Therefore, both the construction of conductive networks and the multiple reflections of EMWs caused by layer structure are vital for the EMI shielding performance of the hydrogels. As the rGO-based hydrogel was frozen at −25 °C, the SE values decreased from ~ 90 to 11.15 dB (Figs. 4(m) and 4(n)). The potent polarization loss capability of water was due to the change of hydrogen bond networks derived from the free movement of polar H_2O. Once the movement of H_2O molecules was limited (such as freezing), the hydrogen bond networks were hard to change under the EM fields, weakening the EMW dissipation loss ability. In addition, without the contribution of water, the corresponding freeze-dried rGO-based aerogels exhibited the EMI SE of only 17.24 dB. Thus, the synergistic effect of the conductive network, polarization loss capability of a water-rich environment, and porous structure led to the efficient EMI shielding performance.

The MXenes with a 2D structure have a high conductivity which is comparable to that of the metals and have been one research topic in EMI shielding [69]. The polar groups and defects on MXene nanosheets could also facilitate the polarization loss of incident EMWs. In addition, the quantities of functional groups on the surface of MXene nanosheets can increase the crosslinking density, contributing to the mechanical properties of hydrogels. Wei et al. fabricated the bioinspired cellulose-integrated MXene-based hydrogels for EMI shielding. With the addition of 10 wt.% MXene, the hydrogels exhibited more than 30 dB with a thickness of 2 mm in the X band [70]. Yu et al. reported the MXene-based PVA/PAAM hydrogel via polymerizing acrylamide (AAm) and connecting the polymers by hydrogen bonds (Figs. 5(a) and 5(b)) [71]. With the increased solvent displacement time, the pore size and thickness of the cell wall of MXene hydrogels decreased (Figs. 5(c) and 5(d)), and the EMI SE firstly increased from 12 to ~ 35 dB with an addition of 1.1 wt.% MXene, and then decreased to ~ 30 dB at a MXene content of 2.2 wt.% (Fig. 5(e)). The non-monotonic change of SE was attributed to the competition between increased electron conduction from MXene and decreased ion conduction. In addition, the decreased cell walls derived from high MXene content were also against the electrical conductivity of networks and multiple reflections of incident EMWs, decreasing the EMI SE. In the practical application, the low-temperature tolerance and anti-drying performance are vital for the hydrogel-based EMI shields. To achieve the long-term stability of hydrogel-based EMI shields, the solvent displacement of MXene-based hydrogel was carried out, and the MXene organic hydrogel containing binary solvent of glycerol (Gly) and water was obtained. After freezing at −25 °C, the SE of MXene organic hydrogel was maintained at more than 30 dB, while the SE of MXene hydrogel declined to 14 dB (Fig. 5(f)). More importantly, during 7-day storage at room temperature, the SE of MXene hydrogel decreased from 30.8 to 1.54 dB, while the SE of MXene organic hydrogel only decreased to 25.3 dB (Figs. 5(g) and 5(h)). However, after the solvent displacement of 60 min, the content of Gly in organic hydrogels further increased, and the EMI SE gradually declined to below 20 dB due to the weak polarization loss of Gly molecules in the GHz band (Fig. 5(i)).

In short, from the above discussion for hydrogel-based EMI shields, the excellent EMI shielding performance of hydrogel-based shields is performed by high conductivity and potent polarization loss derived from conductive nanomaterials and water molecules, respectively, illustrating the equally essential roles of conductive fillers and water-dominated environment.

2.2.2 Hydrogel-based EMI shields integrated with conductive polymers

Although the conductive fillers lift the shielding performance of hydrogels, due to the weak interactions and biocompatibility of inorganic nanomaterials, the compliance, deformability, and biodegradability of hydrogels are compromised [72]. To solve this, employing conductive polymers seems to be an effective strategy to balance the contradiction between conductivity and the mechanical property of hydrogels. Thus, the conducting polymer-based hydrogels have been explored for high-performance EMI shielding.

The PEDOT:PSS, one of the most promising conductive polymers, holds great potential for enabling new EMI-shielding applications due to the intrinsic electrical conductivity [73, 74]. In PEDOT:PSS molecules, the PEDOT contributes to the high electrical conductivity and PSS holds the structure of the polymer as well as improves solubility. Although reducing the content of PSS increases the degree of crystallinity PEDOT and enhances the conductivity, the stability of the PEDOT:PSS polymer chains is impaired. To further lift the conductivity of PEDOT:PSS, Wang et al. utilized the ionic liquid (IL) to modify the PEDOT:PSS polymers for constructing the conductive hydrogels (Fig. 6(a)) [75]. Through the dry-annealing film formation followed by the rehydration method, the conductive polymer hydrogels without conductive inorganic fillers were fabricated. After the modification and rehydration in Gly/water solution, the 50 wt.% ethyl-3-methylimidazolium bis(trifluoromethylsulfonyl)imide (EMIM-TFSI) doped PEDOT:PSS hydrogels ($PEDOT:PSS_{hydrogel}$/EMIM-TFSI) exhibited the conductivity of 30,600 $S \cdot m^{-1}$, which was far higher than that of PEDOT:PSS hydrogels (Fig. 6(b)). This brought about the EMI SE of 53 dB at a thickness of merely 0.045 mm and a thicknesses-normalized SE of 1,182.9 $dB \cdot mm^{-1}$ in the X band (Fig. 6(c)). To achieve accurate customizability, additive manufacturing was employed to prepare the hydrogel-based EMI shields. Liu et al. developed the Ti_3C_2-MXene-modified PEDOT:PSS ink for 3D printing, and a freeze-thawing method was designed to transform the printed objects directly into conductive and robust hydrogels with high shape fidelity (Fig.

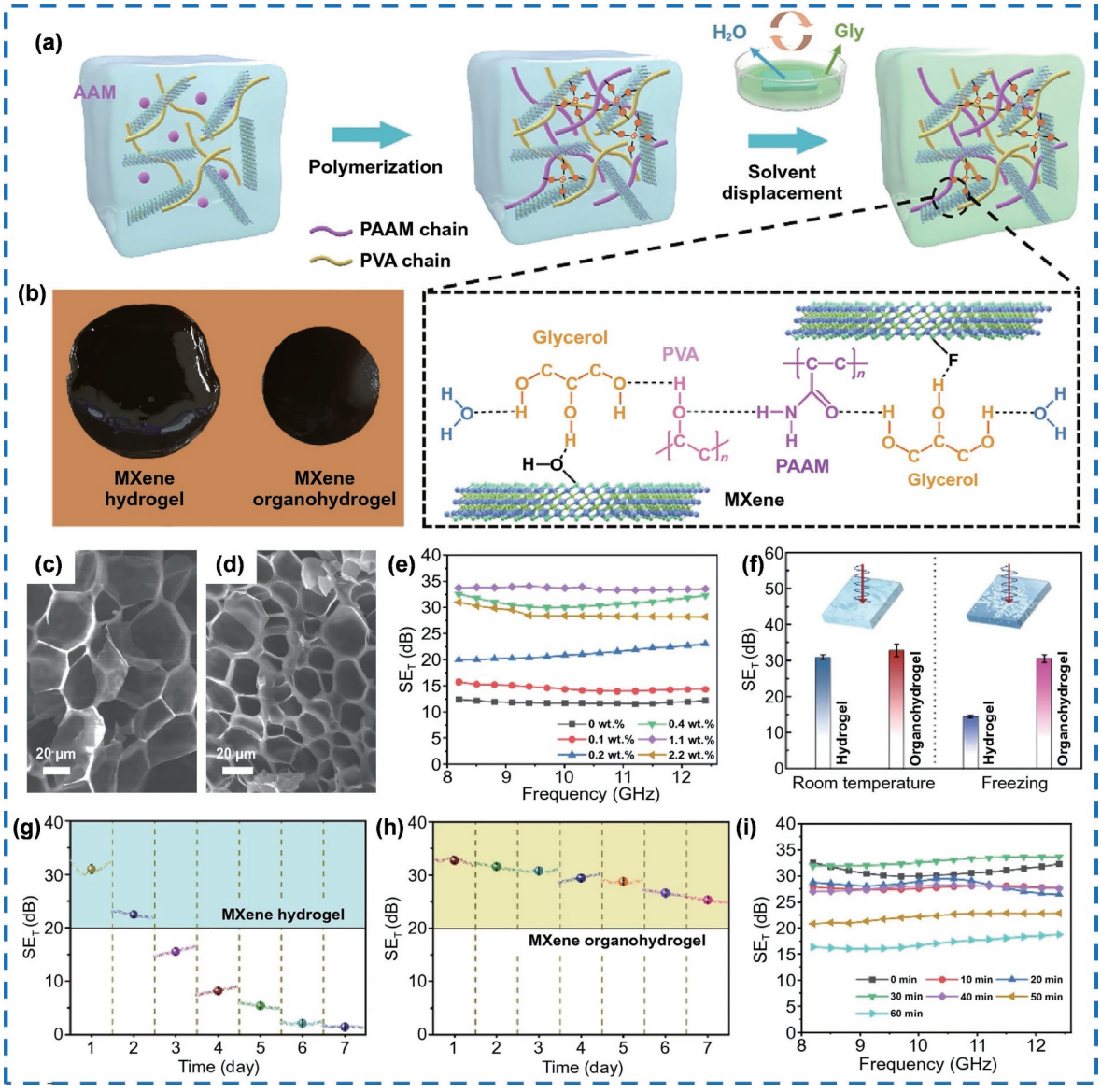

Figure 5 (a) Schematic of preparing MXene-based organic hydrogels, (b) photography of hydrogel and organic hydrogel, (c) and (d) SEM images of porous structures with different displacing time, (e) EMI SE of MXene-based hydrogels, (f) average SE of hydrogel and organic hydrogel before and after freezing, (g) and (h) the stability of hydrogels with storage time, and (i) EMI SE of MXene-based organic hydrogel with water-Gly displacement time. Reproduced with permission from Ref. [71], © Yu, Y. H. et al. 2022.

6(d)) [76]. Dispersing the freeze-dried PEDOT:PSS into MXene dispersion, the inks with optimal printability were simply achieved via adjusting the solid concentration of PEDOT:PSS and MXene to 4 wt.% and 1 wt.%, respectively. The as-printed objects were firstly frozen so that the ice crystals extruded the MXene and PEDOT:PSS to form a framework (Fig. 6(e)). Subsequently, the frozen as-printed objects were thawed in the H_2SO_4 solution immediately. During this process, the partial PSS was dissolved and the crystallinity of PEDOT was increased, increasing the conductivity of hydrogel. After this treatment, the Ti_3C_2-MXene-modified PEDOT:PSS hydrogel with flexibility, stretchability, fatigue resistance, and high fidelity was fabricated (Fig. 6(f)), exhibiting high conductivities of 1,525.8 $S \cdot m^{-1}$ with the water content of 96.6 wt.% to 5,517.2 $S \cdot m^{-1}$ with the water content of 88.86 wt.%. Combined with the high conductivity and water content, the PEDOT:PSS-based hydrogel showed an EMI SE of 51.7 dB at a thickness of 0.295 mm (Figs. 6(g)–6(i)).

2.2.3 *Hydrogel-based EMI shields showing multifunctionalities*

Besides the EMI shielding, emerging multifunctional systems with IoT capabilities such as wearable sensors and thermoelectric conversion are highly desired. Due to the conductivity, flexibility, and biocompatibility, the hydrogels have innate ascendancy in the above functions [77, 78]. By *in situ* polymerizations of acrylamide and N-acryloyl-11-aminoundecanoic acid in AgNWs aerogel (APAA), Huang et al. synthetized conductive APAA hydrogels for EMI shielding and wearable sensor (Figs. 7(a) and 7(b)) [79]. In addition to a 66 dB EMI SE, the hydrogels could be employed to detect the human joint bending sensitively and stably (Figs. 7(c)–7(e)). Besides, the IL-modified PEDOT:PSS hydrogels ($PEDOT:PSS_{hydrogel}$/EMIM-TFSI) obtained by Wang et al. could not only monitor the activity of joint bending [75] but also be acted as thermoelectric generators to output power for hydrogel-based thermoelectric devices, showing application potentials in bioelectric devices as well as wearable organic devices (Figs. 7(f)–7(h)).

In order to highlight the advantages of hydrogel-based EMI shields, Table 1 summarizes the filler content, conductivity, EMI SE, and thickness of the hydrogels. These materials far exceed the basic commercial application requirements (20 dB), and some have also met the needs of multifunctionalities, laying a solid foundation for the EMI shielding application in the future.

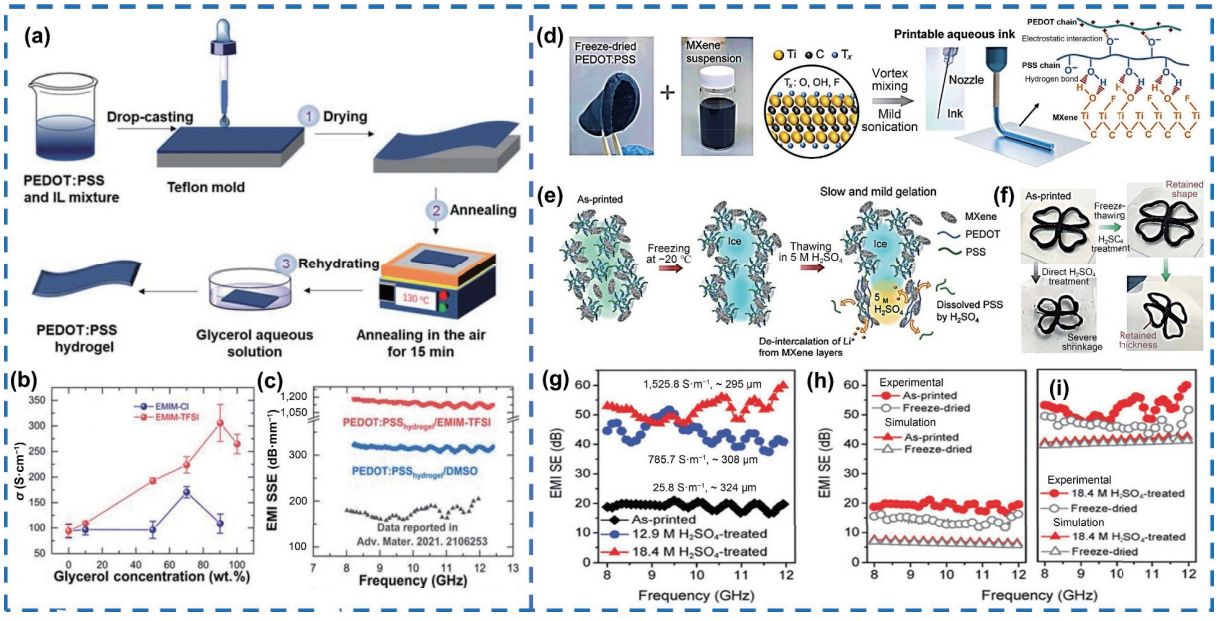

Figure 6 (a) Schematic of preparing IL-doped PEDOT:PSS hydrogel, (b) conductivity of hydrogels varying with the Gly concentration, and (c) EMI SSE of hydrogels. Reproduced with permission from Ref. [75], © Wiley-VCH GmbH 2022. (d) Schematic of preparing MXene/PEDOT:PSS hydrogels via 3D printing, (e) the mechanism of freeze-thawing treatment and (f) high fidelity of hydrogels, (j) EMI SE curves in X band, and (h) and (i) simulated and experimental SE of MXene/PEDOT:PSS hydrogels. Reproduced with permission from Ref. [76], © Wiley-VCH GmbH 2021.

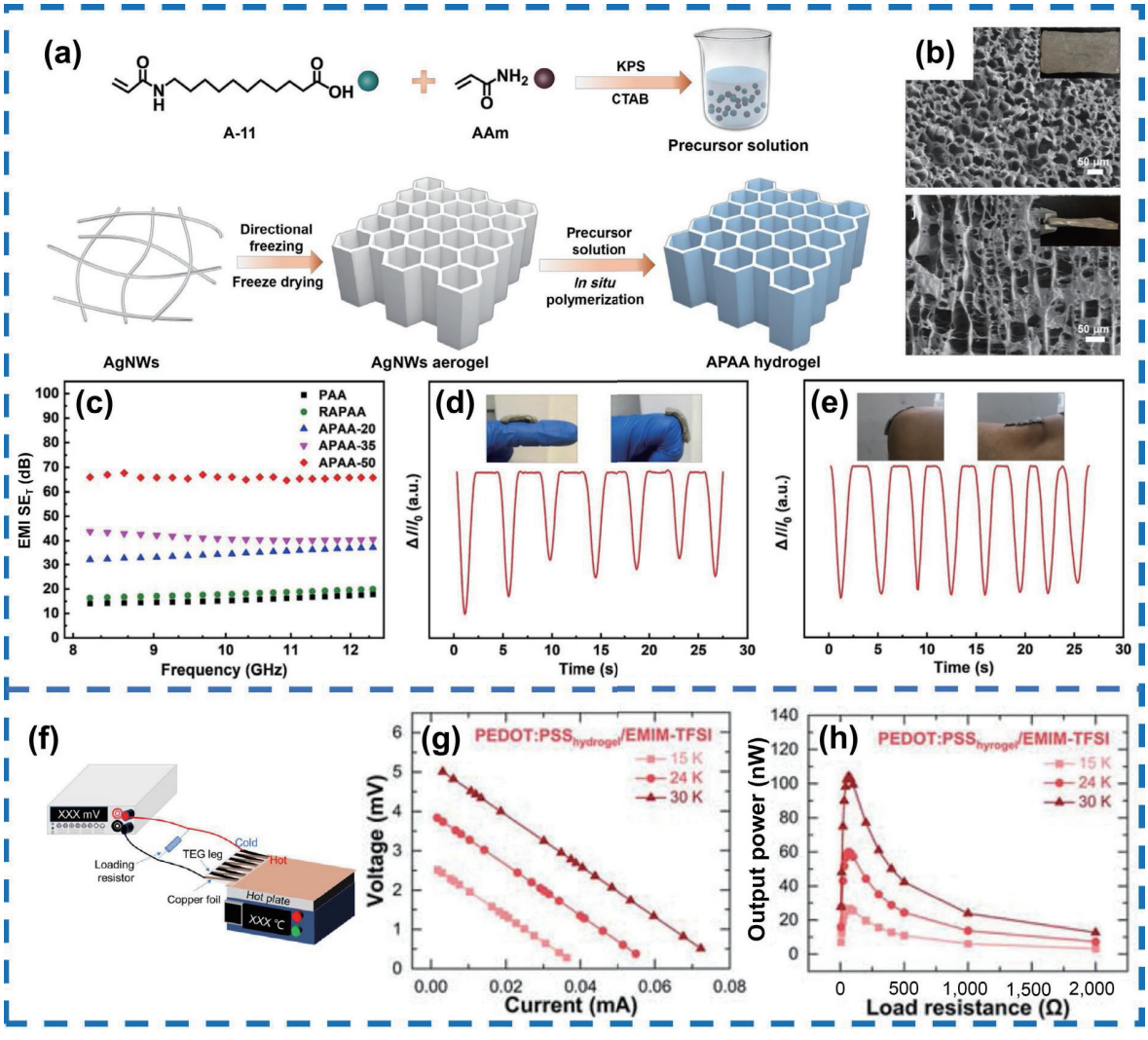

Figure 7 (a) Schematic of constructing APAA hydrogels, (b) the SEM images of porous structure, (c) EMI SE of APAA hydrogels, and (d) and (e) hydrogel as a sensor to detect the human joint bending. Reproduced with permission from Ref. [79], © Elsevier B.V. 2022. (f) Schematic of PEDOT:$PSS_{hydrogel}$/EMIM-TFSI-based thermoelectric generators, (g) voltage–current curves, and (h) generated power of PEDOT:$PSS_{hydrogel}$/EMIM-TFSI at three different temperatures. Reproduced with permission from Ref. [75], © Wiley-VCH GmbH 2022.

Table 1 The shielding performance of hydrogel-based EMI shields

Samples	Filler content	Conductivity (S·m^{-1})	EMI SE (dB)	Thickness (mm)	References
Fe_3O_4/PEDOT:PSS/PVA hydrogel	5 wt.%[b]	0.31	15–46	0.1–1	[53]
ANF-PVA/AgNWs hydrogels	0.02 vol.%–0.23 vol.%	470–16,600	32–52	0.3	[66]
AAm/A-11/AgNWs hydrogel	—	3,700–8,300	66	—	[79]
PAAM/CNF/MWCNT hydrogel	0–1 wt.%[b]	0.12–0.85	16–28.5	2	[68]
CNTs-PAA/CS/ACC hydrogels	4.76 wt.%[a]	—	11–66.5	0.07–9.46	[55]
	0–9.09 wt.%[a]	—	43.14–84.7	9.46	
rGO-PAA/CS/ACC hydrogels	4.76 wt.%[a]	~ 27	20–90	0.04–9.46	[55]
	0–9.09 wt.%[a]	10^{-8}–127.9	49–125	9.46	
IL/PPy/rGO PVA hydrogels	0–3 wt.%[b]	1.5×10^{-5}–8.3×10^{-3} (100 Hz) 1.8×10^{-8}–3.7×10^{-6} (1 THz)	~ 2–32.9 (X band) ~ 10–22.4 (0.2–2 THz)	1	[80]
MXene PAA/ACC hydrogel	6.5 wt.%–12.2 wt.%[a]	0.1–0.8	38.6–52.8 (0.2–2 THz)	0.13	[53]
MXene/PVA organohydrogel	0.1 wt.%–2.2 wt.%[a]	~ 0.099–0.442	14.5–33.6	1	[71]
Cellulose/MXene hydrogel	—	0.0115–0.0188	13.8–30	5	[59]
PEDOT:PSS hydrogel film	—	7.9–20.5	42.7–98.83	0.015–0.228	[73]
MXene/PEDOT:PSS hydrogel	1 wt.%[b]	1,525.8	51.7	0.295	[76]
IL-PEDOT:PSS hydrogel	—	30,600	~ 53	0.045	[75]

[a]Means the concentration of nanomaterials to polymer; [b]indicates the concentration of nanomaterials to hydrogel.

Although hydrogel-based EMI shielding materials have made great strides, some important issues such as the pore structure of the materials are rarely considered. The introduction of ordered and aligned porous structures was beneficial for EMW shielding and absorption in the aerogel-based EMI shields. This may be an inspiration for the future development of high-performance hydrogel-based EMI shields. Therefore, it is necessary to further understand the unique structural design in porous aerogels, especially the biomimetic aligned pore structures, to broaden our research horizons.

3 Porous architectures with biomimetic ordered pores for high-performance EMI shielding

Nowadays, hydrogels with aligned pore structures have emerged in the fields of bioengineering and energy storage materials, but they have not received much attention in the field of EMI shielding. The reason may be that the researchers are unfamiliar with the preparation process of the aligned pore structure and lack of understanding of the EMI shielding mechanism of the aligned pore structure. From this, we attempt to ignite academia's enthusiasm for pore structure design of hydrogel with the introduction of aerogels with biomimetic ordered pore structures.

The design of porous structures plays a crucial role in improving EMI SE [81–85]. Compared with the ordered pore design of hydrogels, there has been a surge in research on aerogels with aligned pore structures [36, 86, 87]. In contrast to the disordered pore structures, ordered or aligned pore structures make aerogels highly anisotropic, which results in unique EMI shielding performance as well as mechanical properties. A huge difference is shown in EMI SE when incident EMWs propagate along the perpendicular direction or parallel direction of aligned pore channels. Multiple reflections of the incident EMWs to the channel walls will be enhanced if the EMWs propagate perpendicular to the aligned pore channels [25, 88]. Meanwhile, the anisotropic pore structures afford [89–91] stronger compressive properties in the specific direction [92–95].

To achieve an aligned pore structure, the template method combined with freeze-drying is a common way [96–99], which is general for ordered pore structure design in hydrogels and aerogels. Song et al. synthesized honeycomb-like rGO/epoxy composite by using Al_2O_3 honeycomb plates as templates. Firstly, the Al_2O_3 template was immersed in graphene oxide (GO) solution, after sonication and standing, the GO sheets would adhere to the surface of Al_2O_3 template. Subsequently, the Al_2O_3 template was completely etched with hydrochloric acid (HCl). Eventually, the GO originally attached to the surface of the Al_2O_3 template would maintain a honeycomb structure. As for EMI shielding performance, honeycomb-like rGO/epoxy composite exhibited an elevated EMI SE of 38 dB [7]. Al_2O_3 templates had the advantages of regular morphology, controllable size and distribution, and good stability. By comparison, the ice templates become more attractive lately, because they are more environmentally friendly and avoid the additional etching process of the templates [26, 100, 101]. Specifically, the ice crystal templates grown under directional freezing will exclude the suspended substance in the aqueous dispersion from the tips of ice crystals to build the cell walls, and then freeze-drying treatment sublimates the ice crystals to form the pore channels [102]. It is worth noting that this preparation technology demonstrates desirable processing flexibility. In detail, the density of the material can be controlled by the amount of water in the suspension. A higher water fraction means greater porosity, which leads to lower density. What's more, various aligned porous structures can be created by setting diverse freezing directions. When unidirectional freezing is applied, the typical aligned cellular structure can be obtained, while aligned lamellar structures are produced under bidirectional freezing.

Previous studies have validated that the aligned pore structures manufactured by ice template method are beneficial to EMI shielding performance [103–105]. Zeng et al. successfully employed MWCNT and water-borne polyurethane (WPU) to prepare lightweight and anisotropic composite foams by the ice-templating freeze-drying method. In addition to the reduced mass density of the composites, the aligned pore structure allowed the EMWs to undergo multiple reflections when the EMWs propagated along the in-plane direction perpendicular to the aligned pore channels. This led to that the in-plane-direction SE_A

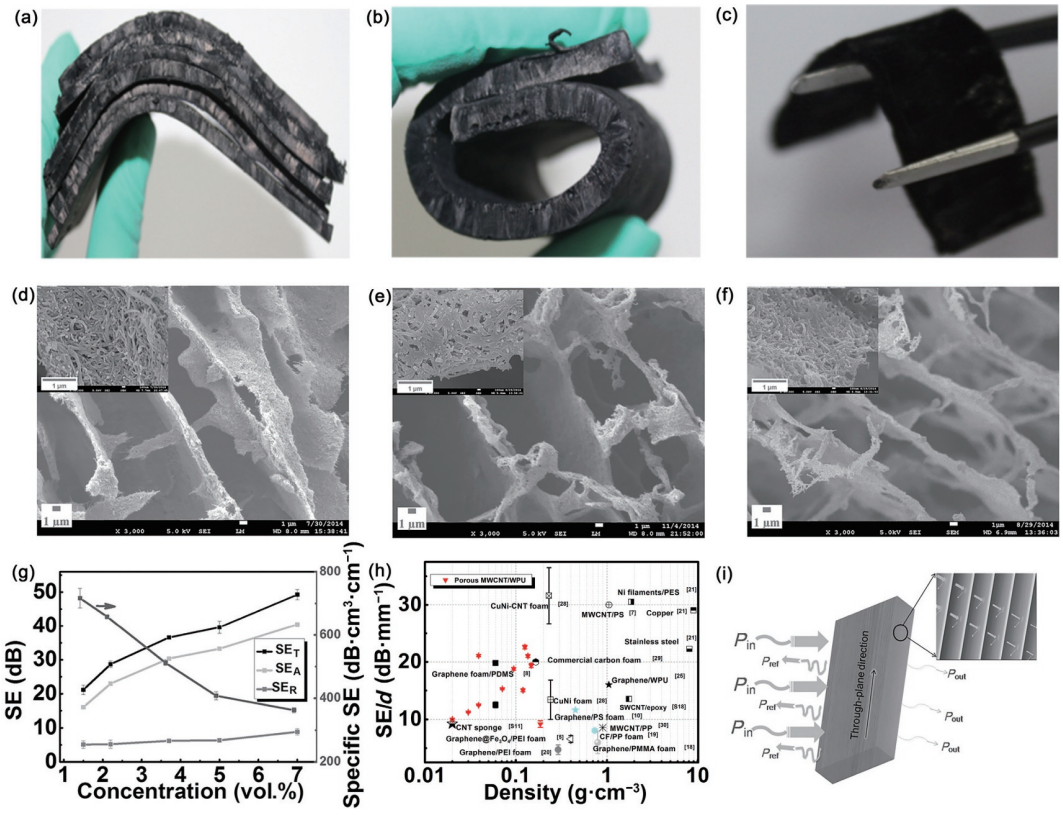

Figure 8 Flexibility of 76.2 wt.% MWCNT/WPU foams with various densities: (a) 126, 95, 71, 39, 30, and 20 (from bottom to top), (b) 70, and (c) 20 mg·cm^{-3}. SEM of 66.7 wt.% MWCNT/WPU foams with various densities: (d) 137, (e) 72, and (f) 29 mg·cm^{-3}. (g) The relationship between MWCNT volume contents and EMI shielding performance of 66.7 wt.% MWCNT/WPU foams at the frequency of 10 GHz. (h) Performance comparison of MWCNT/WPU foams and previously reported materials. (i) The shielding mechanism for the aligned pore structures in the in-plane direction. Reproduced with permission from Ref. [37], © WILEY-VCH Verlag GmbH & Co. KGaA, Weinheim 2015.

was far beyond the through-plane-direction SE_A (Fig. 8). Owing to the unique pore structure, high MWCNT mass ratio, and conductivity of the cell walls, as well as the interfacial polarization of MWCNTs and WPU, the MWCNT/WPU composites can reach a low density of 20 mg·cm^{-3} and a high SE of more than 20 dB. Consequently, a high surface specific SE (SSE/d or SSE/t), defined as the SE divided by the thickness and density by Zeng and his co-workers [37], of 5,410 dB·cm^2·g^{-1} was presented, which far outperformed that of other shielding materials in the same period. Yu and the coworkers applied ice templates to develop anisotropic graphene aerogels (AGA). After AGA was composited with epoxy, the radially incident EMWs along the aligned porous structure obtained significantly enhanced attenuation and reflection [106]. Finally, EMI SE can reach 32 dB along the radial direction.

Furthermore, 3D printing technology with the manufacturing capacity of complex macrostructures and biomass-derived materials is also expected to be a promising option for EMI shielding materials with aligned pore structures [107–109]. Dong et al. reported a 3D freeze-printing (3DFP) method [107], by which complicated 3D MXene aerogel can be yielded. Different from conventional 3D printing, in this work, aqueous MXene dispersion was used as ink and deposited on a –20 °C frozen substrate. Ice as support material facilitates the fabrication of the structures with overhang features. Plus, in terms of microscopic morphology, the aligned channel structure can be observed. Li's team prepared anisotropic carbon monolith with honeycomb structure using cork as a template [109]. This structure not only contributes to good compressive strength (3.3 MPa) but also provides excellent EMI shielding performance (60 dB in X band) due to multiple reflections between cell walls of incident EMWs. Nevertheless, the 3D printing technology requires specific equipment. Simultaneously, the final microstructure of biomass-derived materials depends on the morphology of raw materials, which means that the microstructure of final products is difficult to further tune and optimize. By contrast, the template method, especially the ice-templating approach, is still the most convenient and feasible scheme for the preparation of biomimetic aligned porous architectures.

Recently, an increasing number of aligned pore structures have been developed for EMI shielding. Zhao et al. reported a $Ti_3C_2T_x$ MXene/rGO hybrid aerogels (MGA) with an ordered lattice-like cellular structure [110]. Long-range aligned cell walls were composed of highly conductive MXene and rGO, which was conducive to efficient load transfer and electron transport. Thanks to the conductive network formed by aligned cell walls, the conductivity and EMI SE of the MGA/epoxy composite were 695.9 S·m^{-1} and 56.4 dB with a low MXene content of 0.74 vol.%. MXene was an outstanding EMI shielding material and used to fabricate orderly porous aerogels through bidirectional freeze-casting by Han et al. [20]. On the one hand, the aligned porous structure optimized impedance matching and promoted the multiple reflections of EMWs. On the other hand, MXene has outstanding conductivity as well as plentiful surface terminations and defects intrinsically [111], which leads to strong conduction and polarization losses. Finally, the ultralow density (0.0055 g·cm^{-3}) and high EMI SE (48.5 dB) of MXene aerogels together with an extremely high SSE/d of 88,182 dB·cm^2·g^{-1} were showcased at a thickness of 1 mm. Gao et al. achieved graphene/PDMS composites with high EMI shielding performance at very low graphene content [112]. The bidirectional freezing process imparted a lamellar structure to graphene aerogel, thus achieving anisotropic EMI shielding performance, electrical conductivity, and mechanical properties. Generally, high SE required high

content conductive filler, however, in this work, the ultralow percolation threshold was realized in the long-range aligned composite by structural control. Simultaneously, characteristic aligned structures induced multiple interlayer reflections of incident EMWs. Consequently, a SE of ~ 65 dB and an SSE/*d* of ~100 dB·cm^2·g^{-1} were obtained at a graphene content of ~ 0.42 wt.%. Gu and his coworkers reported the rGO@FeNi/epoxy composites with regular honeycomb structure (rGH@FeNi/epoxy) [113]. A highly oriented hexagonal honeycomb structure facilitated the formation of continuous conductive networks and enhanced the mechanical properties of the rGH@FeNi/epoxy. Besides, FeNi and epoxy contributed to the impedance matching. Eventually, rGH@FeNi/epoxy composites showcased the high EMI SE of 46 dB at a low rGH@FeNi mass fraction of 2.1 wt.%.

Apart from typical carbon materials [114–117], some emerging biopolymers have also been applied to promote the construction of aligned porous architectures. For instance, green and renewable nanocellulose is widely recognized for its high strength-to-weight ratio, large aspect ratio, and large specific surface area. Meanwhile, abundant functional groups and numerous amphiphilic faces are more noteworthy. These advantages make the nanocellulose have excellent dispersibility and good interaction with various nanomaterials, so that nanocellulose can load many kinds of nanomaterials to construct stable porous hydrogel/aerogel composites. Lu and his coworkers manufactured a kind of 3D unidirectional porous aerogels based on lignin-derived carbon (LDC) and rGO [118]. LDC could serve as the "binder" between GO layers to facilitate the assembly of composite aerogels with well-aligned pore structures. Interestingly, due to the aligned pore structure, the transversely incident EMWs had more interactions with the pore walls, resulting in a potent SE_A and thus a high SE_T. Finally, the SSE/*d* (53,250 dB·cm^2·g^{-1}) surpassing that of other reported carbon-based and even metal-based shielding materials was obtained (Fig. 9).

Fei et al. combined zeolitic imidazolate framework (ZIF)-67 and CNF to prepare Co/C@CNF aerogels [119]. The carbonized CNF could act as a continuous conductive network and form an aligned honeycomb structure, which provided effective surfaces for multiple reflections and scatterings of EMWs. In the meanwhile, the embedded Co/C nanoparticles optimized impedance matching and induced multi-interface polarization. Eventually, the Co/C@CNF aerogel reached an EMI SE of around 35.1 dB at a density of 1.74 mg·cm^{-3}, and the corresponding SSE was 20,172.4 dB·cm^3·g^{-1}. Wang et al. also reported the enhancement in EMI SE of CNF/MXene aerogels (CTA) with aligned porous structure [120]. After annealing, anisotropic morphology could be well preserved (Fig. 10). With the impregnating of epoxy resins, the CTA/epoxy composites could achieve the electrical conductivity of 1,672 S·m^{-1} and an EMI SE of 74 dB at a volume fraction of MXene of 1.38 vol.%.

Zeng et al. fabricated a series of CNF/AgNWs aerogels [21]. Notably, the difference in EMI shielding performance among the nacre-like lamellar microstructures, honeycomb-like cellular microstructures, and randomly porous structures was taken into consideration. The different morphologies were realized by regulating the direction of freezing. In terms of nacre-like lamellar microstructures, freezing in both horizontal and vertical directions is required to allow flake ice crystals to form and grow. As for honeycomb-like and randomly porous structures, they just require

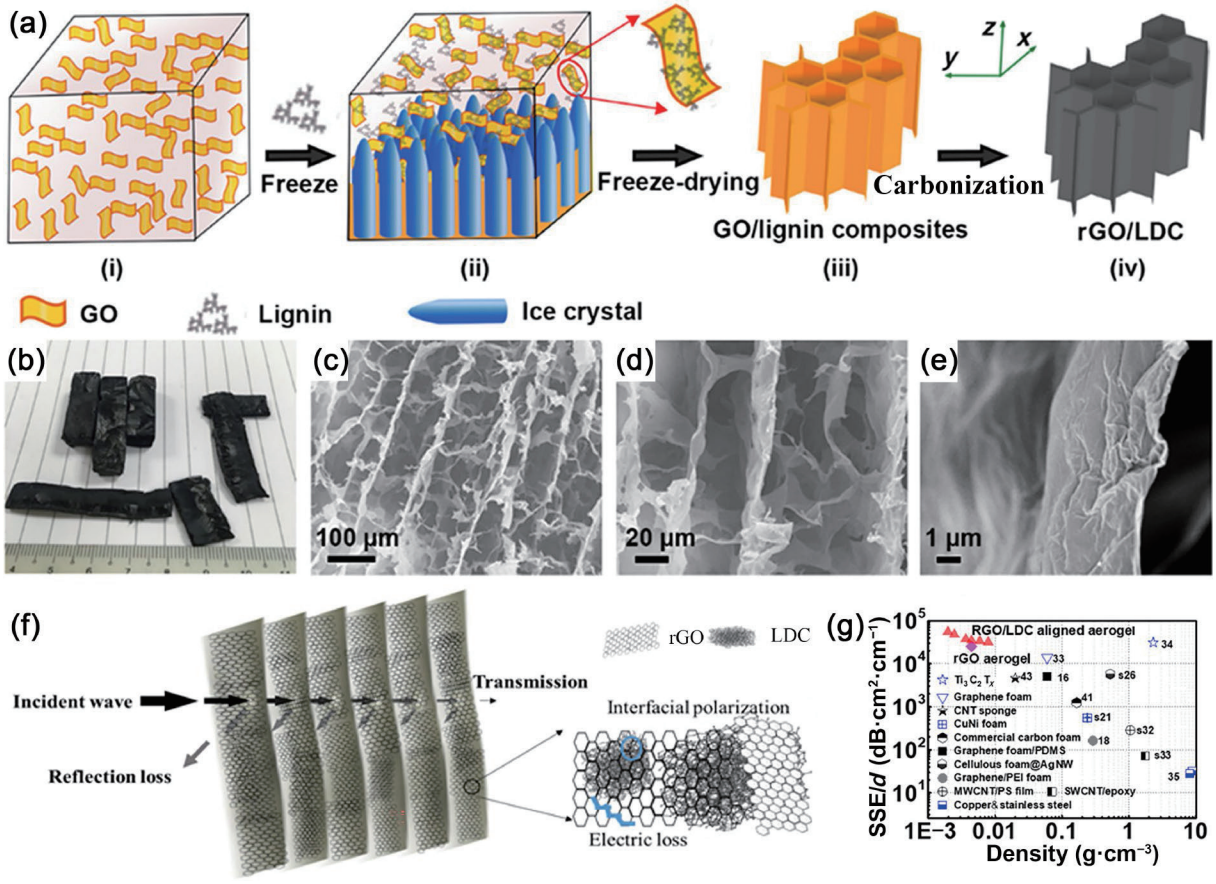

Figure 9 (a) Fabrication process of rGO/LDC aerogels: (i) GO aqueous dispersion, (ii) freezing process, (iii) GO/lignin composite foam, and (iv) rGO/LDC aerogel (*Z* was defined as the longitudinal direction, while *X* and *Y* were defined as transverse directions). (b) Digital photo of rGO/LDC aerogels after carbonization with various shapes. (c)–(e) Transverse SEM images of rGO/LDC aerogels. (f) Proposed EMI shielding mechanism for the rGO/LDC aerogels with the incident wave in the transverse direction. (g) SSE/*d* as a function of density compared with previous reported shielding materials. Reproduced with permission from Ref. [118], © American Chemical Society 2018.

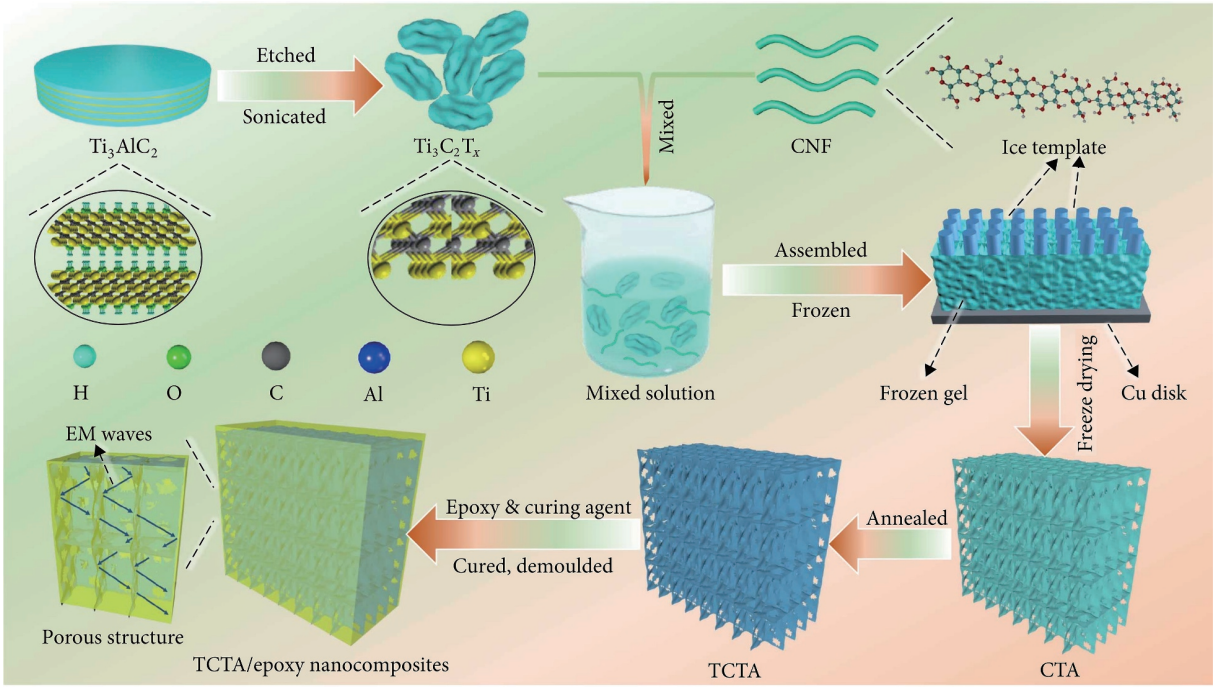

Figure 10 Schematic diagram of manufacturing process of TCTA/epoxy nanocomposites. Reproduced with permission from Ref. [120], © Wang, L. et al. 2020.

to control the growth of ice crystals in single or random direction. The experimental results showed that the maximum SE_A can be obtained when incident EMWs propagated along the direction perpendicular to the nacre-like lamellar pore channels (Figs. 11(a)–11(f)), which could be explained by the maximum number of multiple reflections of EMWs and more interactions of EMWs with pore walls. Moreover, CNFs with high aspect ratio and large specific surface area could interact with highly conductive AgNWs for the assembly of composite aerogels with high mechanical strength, flexibility, and conductivity, as well as low density. The optimized sample exhibited a very high EMI SE exceeding 40 dB in the X-band, while the density of the CNFs/AgNWs aerogel was as low as 1.7 mg·cm^{-3}. More impressively, the SSE/d could reach 178,235 dB·cm^2·g^{-1}, which was far superior to that of other shielding materials ever reported. Therefore, jointly with the high EMW reflection and absorption capacity of the pore walls, the aligned porous channel structures contributed to the outstanding EMI shielding performance of the composite aerogels. Subsequently, the relationship between the propagation direction of EMWs and EMI shielding performance based on the aligned pore structures was further studied [69]. Lamellar MXene/CNF aerogels were developed through a bidirectional freeze-drying method. The MXene/CNF aerogels presented large-scale parallel-oriented cell walls. The angle (φ) between the lamellar cell walls and the electric field direction of the incident EMWs was proven to be closely related to the EMI shielding performance (Figs. 11(g)–11(k)). It followed that EMI SE increased from 36.5 to 63.1 dB as the φ increased from 0° to 90°, which means that the loss of EMWs becomes tunable by changing φ. The reason was that the interior of the cell walls with abundant heterointerfaces and high conductivity would form an interior electric field induced by the external electromagnetic field. At the φ of 0°, cell walls were all parallel to the external electric field, thus causing a high interior electric field accompanied by the highest SE_T and SE_A. This result illustrated the significant dependency between aligned pore structures and EMW shielding and absorption [121, 122]. At the same time, it is also worth noting that by combining highly conductive cell walls with aligned pore structures, the MXene/CNF aerogel realized an eye-catching SSE/d up to 189,400 dB·cm^2·g^{-1}.

From the above discussions, it is clear that the positive effect of aligned porous structures on EMI shielding is widely recognized. Notwithstanding the EMI shields presented in this section belong to aerogels rather than hydrogels, the EMI shielding mechanism of the ordered pore structure is universal. Some works provide key insights into the EMI shielding mechanism of aligned porous structure. In simple terms, on the one hand, the aligned porous structure may provide more multiple reflections, and on the other hand, the anisotropic porous structures may also form a strong internal electric field induced by electric field of incident EMWs to dissipate the energy of EMWs. This mechanism is also expected to be used to guide the rational pore structure design of hydrogels. Thus, the introduction of the biomimetic ordered pore structures in this section aims to emphasize the importance of rational pore structure and provide a new perspective for the further development of hydrogel-based EMI shields.

4 Conclusions and outlook

In this review, the fabrication methods and the latest research progress for hydrogel-based EMI shielding materials in recent years were reviewed. Benefiting from the tough crosslinking between polymers derived from widely used physical and chemical cross-linking methods, the hydrogels possess mechanical ultra-flexibility and stretchability beyond the traditional porous materials. Hydrogel-based EMI shields with various inorganic conductive fillers or conductive polymer networks demonstrated excellent EMI shielding performance. In addition, due to the conductivity, flexibility, and biocompatibility, the multifunctionalities of hydrogel materials also contributed to a promising application prospect. To inspire the development of porous hydrogels and illustrate the effect of pore microstructure on shielding performance, the porous EMI shields with biomimetic aligned pore structures were also mentioned in this review. The further understanding of the relationships between EMI shielding performance and aligned pore structure was introduced, which may promote the subsequent design of hydrogel-based high-performance EMI shielding materials. Conceivably, hydrogels with pore structure design will be desirable next-generation EMI shielding materials.

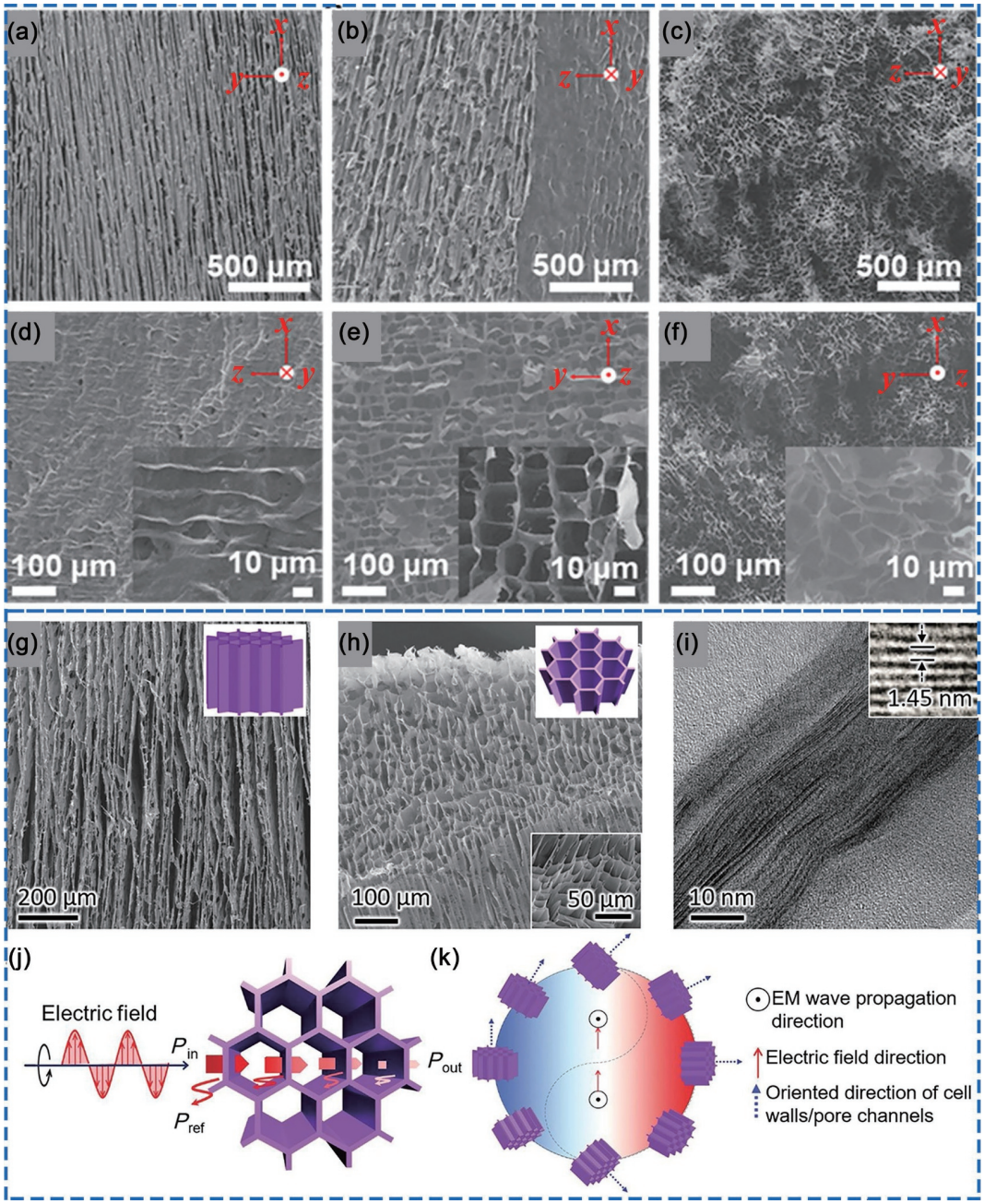

Figure 11 SEM images of the CNF/AgNW aerogels: (a) and (d) nacre-like lamellar microstructures, (b) and (e) honeycomb-like cellular microstructures, and (c) and (f) random porous structures. Reproduced with permission from Ref. [21], © American Chemical Society 2020. SEM images of the (g) longitudinal plane and (h) transverse plane for the MXene/CNF hybrid aerogels with 17 wt.% CNF and density of 4 mg·cm^{-3}. (i) Cross-sectional TEM images of the corresponding MXene/CNF hybrid cell walls. (j) The EMI shielding mechanism when the incident EM waves propagate in the transverse direction, showing the most multi-reflections of EM waves in this direction. (k) Proposed cell walls'/pore channels' orientation-induced EMI shielding mechanism. Reproduced with permission from Ref. [69], © Zeng, Z. H. et al. 2020.

Although the researchers have made decent progress in exploring the EMI shielding performance, there are still several issues that are not involved. First, the controllable morphology of micrometer-sized pores such as aligned channels and anisotropic pore structure, which have been proven to efficiently improve the EMI shielding performance of porous materials [40, 68, 70], is not considered for the current hydrogel-based EMI shields. In addition, apart from the EMI shielding, the attempts of hydrogels in the multifunctional applications are barely carried out, which does not fully utilize the superiorities in mechanical properties and biocompatibility of the hydrogels. Thus, we suggest that illuminating and further understanding the relationships between controllable interior porous structures, components, and EMI shielding performance should be the priority in hydrogel-based EMI shields. It is believed that if hydrogel-based shielding materials are combined with the design of controllable pore structures, they will be more promising for high-performance EMI shielding materials. In the meanwhile, the multifunctionalities such as photothermal therapy, antisepsis coating, and adhesiveness should be paid more attention to extend the application potential of hydrogel-based EMI shields.

Acknowledgements

This work was supported by the Provincial Key Research and Development Program of Shandong (Nos. 2019JZZY010312 and 2021ZLGX01), New 20 Funded Programs for Universities of Jinan (No. 2021GXRC036), and Shenzhen municipal special fund for guiding local scientific and technological development (No. China

2021Szvup071).

Funding note: Open Access funding provided by Swiss Federal Institute of Technology Zurich.

References

[1] Thomassin, J. M.; Jérôme, C.; Pardoen, T.; Bailly, C.; Huynen, I.; Detrembleur, C. Polymer/carbon based composites as electromagnetic interference (EMI) shielding materials. *Mater. Sci. Eng. R Rep.* **2013**, *74*, 211–232.

[2] Liu, J.; Zhang, H. B.; Sun, R. H.; Liu, Y. F.; Liu, Z. S.; Zhou, A. G.; Yu, Z. Z. Hydrophobic, flexible, and lightweight MXene foams for high-performance electromagnetic-interference shielding. *Adv. Mater.* **2017**, *29*, 1702367.

[3] Cheng, Y.; Li, X. Y.; Qin, Y. X.; Fang, Y. T.; Liu, G. L.; Wang, Z. Y.; Matz, J.; Dong, P.; Shen, J. F.; Ye, M. X. Hierarchically porous polyimide/$Ti_3C_2T_x$ film with stable electromagnetic interference shielding after resisting harsh conditions. *Sci. Adv.* **2021**, *7*, eabj1663.

[4] Wu, N.; Zeng, Z. H.; Kummer, N.; Han, D. X.; Zenobi, R.; Nyström, G. Ultrafine cellulose nanofiber-assisted physical and chemical cross-linking of MXene sheets for electromagnetic interference shielding. *Small Methods* **2021**, *5*, 2100889.

[5] Zeng, Z. H.; Wu, N.; Wei, J. J.; Yang, Y. F.; Wu, T. T.; Li, B.; Hauser, S. B.; Yang, W. D.; Liu, J. R.; Zhao, S. Y. Porous and ultra-flexible crosslinked MXene/polyimide composites for multifunctional electromagnetic interference shielding. *Nano-Micro Lett.* **2022**, *14*, 59.

[6] Shi, S. W.; Qian, B. Q.; Wu, X. Y.; Sun, H. L.; Wang, H. Q.; Zhang, H. B.; Yu, Z. Z.; Russell, T. P. Self-assembly of MXene-surfactants at liquid–liquid interfaces: From structured liquids to 3D aerogels. *Angew. Chem., Int. Ed.* **2019**, *58*, 18171–18176.

[7] Song, P.; Liang, C. B.; Wang, L.; Qiu, H.; Gu, H. B.; Kong, J.; Gu, J. W. Obviously improved electromagnetic interference shielding performances for epoxy composites via constructing honeycomb structural reduced graphene oxide. *Compos. Sci. Technol.* **2019**, *181*, 107698.

[8] Chen, W.; Liu, L. X.; Zhang, H. B.; Yu, Z. Z. Kirigami-inspired highly stretchable, conductive, and hierarchical $Ti_3C_2T_x$ MXene films for efficient electromagnetic interference shielding and pressure sensing. *ACS Nano* **2021**, *15*, 7668–7681.

[9] Hu, P. Y.; Lyu, J.; Fu, C.; Gong, W. B.; Liao, J. H.; Lu, W. B.; Chen, Y. P.; Zhang, X. T. Multifunctional aramid nanofiber/carbon nanotube hybrid aerogel films. *ACS Nano* **2020**, *14*, 688–697.

[10] Wei, Q. W.; Pei, S. F.; Qian, X. T.; Liu, H. P.; Liu, Z. B.; Zhang, W. M.; Zhou, T. Y.; Zhang, Z. C.; Zhang, X. F.; Cheng, H. M. et al. Superhigh electromagnetic interference shielding of ultrathin aligned pristine graphene nanosheets film. *Adv. Mater.* **2020**, *32*, 1907411.

[11] Chen, Y. M.; Yang, Y.; Xiong, Y.; Zhang, L.; Xu, W. H.; Duan, G. G.; Mei, C. T.; Jiang, S. H.; Rui, Z. H.; Zhang, K. Porous aerogel and sponge composites: Assisted by novel nanomaterials for electromagnetic interference shielding. *Nano Today* **2021**, *38*, 101204.

[12] Yang, R. L.; Gui, X. C.; Yao, L.; Hu, Q. M.; Yang, L. L.; Zhang, H.; Yao, Y. T.; Mei, H.; Tang, Z. K. Ultrathin, lightweight, and flexible CNT buckypaper enhanced using MXenes for electromagnetic interference shielding. *Nano-Micro Lett.* **2021**, *13*, 66.

[13] Weng, G. M.; Li, J. Y.; Alhabeb, M.; Karpovich, C.; Wang, H.; Lipton, J.; Maleski, K.; Kong, J.; Shaulsky, E.; Elimelech, M. et al. Layer-by-Layer assembly of cross-functional semi-transparent MXene-carbon nanotubes composite films for next-generation electromagnetic interference shielding. *Adv. Funct. Mater.* **2018**, *28*, 1803360.

[14] Kong, L.; Yin, X. W.; Xu, H. L.; Yuan, X. Y.; Wang, T.; Xu, Z. W.; Huang, J. F.; Yang, R.; Fan, H. Powerful absorbing and lightweight electromagnetic shielding CNTs/RGO composite. *Carbon* **2019**, *145*, 61–66.

[15] Zhang, Y.; Huang, Y.; Zhang, T. F.; Chang, H. C.; Xiao, P. S.; Chen, H. H.; Huang, Z. Y.; Chen, Y. S. Broadband and tunable high-performance microwave absorption of an ultralight and highly compressible graphene foam. *Adv. Mater.* **2015**, *27*, 2049–2053.

[16] Ma, T. B.; Ma, H.; Ruan, K. P.; Shi, X. T.; Qiu, H.; Gao, S. Y.; Gu, J. W. Thermally conductive poly(lactic acid) composites with superior electromagnetic shielding performances via 3D printing technology. *Chin. J. Polym. Sci.* **2022**, *40*, 248–255.

[17] Zhang, Y. L.; Ma, Z. L.; Ruan, K. P.; Gu, J. W. Flexible $Ti_3C_2T_x$/(aramid nanofiber/PVA) composite films for superior electromagnetic interference shielding. *Research* **2022**, *2022*, 9780290.

[18] Wang, L.; Ma, Z. L.; Zhang, Y. L.; Qiu, H.; Ruan, K. P.; Gu, J. W. Mechanically strong and folding-endurance $Ti_3C_2T_x$ MXene/PBO nanofiber films for efficient electromagnetic interference shielding and thermal management. *Carbon Energy* **2022**, *4*, 200–210.

[19] Zhang, Y. L.; Ruan, K. P.; Gu, J. W. Flexible sandwich-structured electromagnetic interference shielding nanocomposite films with excellent thermal conductivities. *Small* **2021**, *17*, 2101951.

[20] Han, M. K.; Yin, X. W.; Hantanasirisakul, K.; Li, X. L.; Iqbal, A.; Hatter, C. B.; Anasori, B.; Koo, C. M.; Torita, T.; Soda, Y. et al. Anisotropic MXene aerogels with a mechanically tunable ratio of electromagnetic wave reflection to absorption. *Adv. Opt. Mater.* **2019**, *7*, 1900267.

[21] Zeng, Z. H.; Wu, T. T.; Han, D. X.; Ren, Q.; Siqueira, G.; Nyströem, G. Ultralight, flexible, and biomimetic nanocellulose/silver nanowire aerogels for electromagnetic interference shielding. *ACS Nano* **2020**, *14*, 2927–2938.

[22] Han, Y. X.; Ruan, K. P.; Gu, J. W. Janus (BNNS/ANF)-(AgNWs/ANF) thermal conductivity composite films with superior electromagnetic interference shielding and Joule heating performances. *Nano Res.* **2022**, *15*, 4747–4755.

[23] Wang, L.; Ma, Z. L.; Zhang, Y. L.; Chen, L. X.; Cao, D. P.; Gu, J. W. Polymer-based EMI shielding composites with 3D conductive networks: A mini-review. *SusMat* **2021**, *1*, 413–431.

[24] Zeng, Z. H.; Qiao, J.; Zhang, R. N.; Liu, J. R.; Nyström, G. Nanocellulose-assisted preparation of electromagnetic interference shielding materials with diversified microstructure. *SmartMat*, in press, https://doi.org/10.1002/smm2.1118.

[25] Zhang, L. Q.; Yang, S. G.; Li, L.; Yang, B.; Huang, H. D.; Yan, D. X.; Zhong, G. J.; Xu, L.; Li, Z. M. Ultralight cellulose porous composites with manipulated porous structure and carbon nanotube distribution for promising electromagnetic interference shielding. *ACS Appl. Mater. Interfaces* **2018**, *10*, 40156–40167.

[26] Chen, Y. W.; Zhang, H. Y.; Zeng, G. X. Tunable and high performance electromagnetic absorber based on ultralight 3D graphene foams with aligned structure. *Carbon* **2018**, *140*, 494–503.

[27] Yang, Y. L.; Gupta, M. C.; Dudley, K. L.; Lawrence, R. W. Novel carbon nanotube-polystyrene foam composites for electromagnetic interference shielding. *Nano Lett.* **2005**, *5*, 2131–2134.

[28] Chen, Y. A.; Pötschke, P.; Pionteck, J.; Voit, B.; Qi, H. S. Multifunctional cellulose/rGO/Fe_3O_4 composite aerogels for electromagnetic interference shielding. *ACS Appl. Mater. Interfaces*

2020, *12*, 22088–22098.
[29] Jaspers, M.; Rowan, A. E.; Kouwer, P. H. J. Tuning hydrogel mechanics using the hofmeister effect. *Adv. Funct. Mater.* **2015**, *25*, 6503–6510.
[30] Sano, K.; Ishida, Y.; Aida, T. Synthesis of anisotropic hydrogels and their applications. *Angew. Chem., Int. Ed.* **2018**, *57*, 2532–2543.
[31] Zhan, Z. Y.; Song, Q. C.; Zhou, Z. H.; Lu, C. H. Ultrastrong and conductive MXene/cellulose nanofiber films enhanced by hierarchical nano-architecture and interfacial interaction for flexible electromagnetic interference shielding. *J. Mater. Chem. C* **2019**, *7*, 9820–9829.
[32] Zeng, Z. H.; Wang, C. X.; Wu, T. T.; Han, D. X.; Luković, M.; Pan, F.; Siqueira, G.; Nyström, G. Nanocellulose assisted preparation of ambient dried, large-scale and mechanically robust carbon nanotube foams for electromagnetic interference shielding. *J. Mater. Chem. A* **2020**, *8*, 17969–17979.
[33] Hogg, D. C.; Guiraud, F. O. Microwave measurements of the absolute values of absorption by water vapour in the atmosphere. *Nature* **1979**, *279*, 408–409.
[34] Buchner, R.; Barthel, J.; Stauber, J. The dielectric relaxation of water between 0 °C and 35 °C. *Chem. Phys. Lett.* **1999**, *306*, 57–63.
[35] Garner, H. R.; Ohkawa, T.; Tuason, O.; Lee, R. L. Microwave absorption in substances that form hydration layers with water. *Phys. Rev. A* **1990**, *42*, 7264–7270.
[36] Zhu, M.; Yan, X. X.; Xu, H. L.; Xu, Y. J.; Kong, L. Ultralight, compressible, and anisotropic MXene@wood nanocomposite aerogel with excellent electromagnetic wave shielding and absorbing properties at different directions. *Carbon* **2021**, *182*, 806–814.
[37] Zeng, Z. H.; Jin, H.; Chen, M. J.; Li, W. W.; Zhou, L. C.; Zhang, Z. Lightweight and anisotropic porous MWCNT/WPU composites for ultrahigh performance electromagnetic interference shielding. *Adv. Funct. Mater.* **2016**, *26*, 303–310.
[38] Song, P.; Qiu, H.; Wang, L.; Liu, X. Y.; Zhang, Y. L.; Zhang, J. L.; Kong, J.; Gu, J. W. Honeycomb structural rGO-MXene/epoxy nanocomposites for superior electromagnetic interference shielding performance. *Sustain. Mater. Technol.* **2020**, *24*, e00153.
[39] Liu, X. M.; Liu, H. Q.; Xu, H. L.; Xie, W. J.; Li, M. H.; Liu, J. X.; Liu, G. Q.; Weidenkaff, A.; Riedel, R. Natural wood templated hierarchically cellular NbC/pyrolytic carbon foams as stiff, lightweight and high-performance electromagnetic shielding materials. *J. Colloid Interf. Sci.* **2022**, *606*, 1543–1553.
[40] Zeng, Z. H.; Jin, H.; Chen, M. J.; Li, W. W.; Zhou, L. C.; Xue, X.; Zhang, Z. Microstructure design of lightweight, flexible, and high electromagnetic shielding porous multiwalled carbon nanotube/polymer composites. *Small* **2017**, *13*, 1701388.
[41] Zhang, Y. S.; Khademhosseini, A. Advances in engineering hydrogels. *Science* **2017**, *356*, eaaf3627.
[42] Seliktar, D. Designing cell-compatible hydrogels for biomedical applications. *Science* **2012**, *336*, 1124–1128.
[43] Andryieuski, A.; Kuznetsova, S. M.; Zhukovsky, S. V.; Kivshar, Y. S.; Lavrinenko, A. V. Water: Promising opportunities for tunable all-dielectric electromagnetic metamaterials. *Sci. Rep.* **2015**, *5*, 13535.
[44] King, G. W.; Hainer, R. M.; Cross, P. C. Expected microwave absorption coefficients of water and related molecules. *Phys. Rev.* **1947**, *71*, 433–443.
[45] Ahmed, E. M. Hydrogel: Preparation, characterization, and applications: A review. *J. Adv. Res.* **2015**, *6*, 105–121.
[46] Zainal, S. H.; Mohd, N. H.; Suhaili, N.; Anuar, F. H.; Lazim, A. M.; Othaman, R. Preparation of cellulose-based hydrogel: A review. *J. Mater. Res. Technol.* **2021**, *10*, 935–952.
[47] Hamedi, H.; Moradi, S.; Hudson, S. M.; Tonelli, A. E. Chitosan based hydrogels and their applications for drug delivery in wound dressings: A review. *Carbohydr. Polym.* **2018**, *199*, 445–460.
[48] Thoniyot, P.; Tan, M. J.; Karim, A. A.; Young, D. J.; Loh, X. J. Nanoparticle-hydrogel composites: Concept, design, and applications of these promising, multi-functional materials. *Adv. Sci.* **2015**, *2*, 1400010.
[49] Wang, L. R.; Xu, T. L.; Zhang, X. J. Multifunctional conductive hydrogel-based flexible wearable sensors. *TrAC-Trend. Anal. Chem.* **2021**, *134*, 116130.
[50] Distler, T.; Boccaccini, A. R. 3D printing of electrically conductive hydrogels for tissue engineering and biosensors—A review. *Acta Biomater.* **2020**, *101*, 1–13.
[51] Timofejeva, A.; D'Este, M.; Loca, D. Calcium phosphate/polyvinyl alcohol composite hydrogels: A review on the freeze-thawing synthesis approach and applications in regenerative medicine. *Eur. Polym. J.* **2017**, *95*, 547–565.
[52] Zhang, Y.; Cremer, P. S. Interactions between macromolecules and ions: The Hofmeister series. *Curr. Opin. Chem. Biol.* **2006**, *10*, 658–663.
[53] Hao, M. M.; Wang, Y. F.; Li, L. H.; Lu, Q. F.; Sun, F. Q.; Li, L. L.; Yang, X. Q.; Li, Y.; Liu, M. Y.; Feng, S. J. et al. Stretchable multifunctional hydrogels for sensing electronics with effective EMI shielding properties. *Soft Matter* **2021**, *17*, 9057–9065.
[54] Hu, W. K.; Wang, Z. J.; Xiao, Y.; Zhang, S. M.; Wang, J. L. Advances in crosslinking strategies of biomedical hydrogels. *Biomater. Sci.* **2019**, *7*, 843–855.
[55] Lai, D. G.; Chen, X. X.; Wang, G.; Xu, X. H.; Wang, Y. Arbitrarily reshaping and instantaneously self-healing graphene composite hydrogel with molecule polarization-enhanced ultrahigh electromagnetic interference shielding performance. *Carbon* **2022**, *188*, 513–522.
[56] Wan, S. J.; Li, X.; Wang, Y. L.; Chen, Y.; Xie, X.; Yang, R.; Tomsia, A. P.; Jiang, L.; Cheng, Q. F. Strong sequentially bridged MXene sheets. *Proc. Natl. Acad. Sci. USA* **2020**, *117*, 27154–27161.
[57] Zhu, Y. Y.; Liu, J.; Guo, T.; Wang, J. J.; Tang, X. Z.; Nicolosi, V. Multifunctional $Ti_3C_2T_x$ MXene composite hydrogels with strain sensitivity toward absorption-dominated electromagnetic-interference shielding. *ACS Nano* **2021**, *15*, 1465–1474.
[58] Bai, Y.; Bi, S. H.; Wang, W. K.; Ding, N.; Lu, Y. Y.; Jiang, M. Y.; Ding, C. B.; Zhao, W. W.; Liu, N.; Bian, J. et al. Biocompatible, stretchable, and compressible cellulose/MXene hydrogel for strain sensor and electromagnetic interference shielding. *Soft Mater.*, in press, https://doi.org/10.1080/1539445X.2022.2081580.
[59] Udoetok, I. A.; Dimmick, R. M.; Wilson, L. D.; Headley, J. V. Adsorption properties of cross-linked cellulose-epichlorohydrin polymers in aqueous solution. *Carbohydr. Polym.* **2016**, *136*, 329–340.
[60] Wu, S. Q.; Chen, D. M.; Han, W. B.; Xie, Y. S.; Zhao, G. D.; Dong, S.; Tan, M. Y.; Huang, H.; Xu, S. B.; Chen, G. Q. et al. Ultralight and hydrophobic MXene/chitosan-derived hybrid carbon aerogel with hierarchical pore structure for durable electromagnetic interference shielding and thermal insulation. *Chem. Eng. J.* **2022**, *446*, 137093.
[61] Zhao, X.; Guo, D. M.; An, Q. D.; Bo, S. F.; Xiao, Z. Y.; Cai, W. J.; Wang, H. S.; Zhai, S. R.; Li, Z. C. Hierarchical nitrogen/cobalt co-doped carbonaceous materials with electromagnetic waves absorption promoting nanostructures. *J. Alloys Compd.* **2020**, *822*, 153666.
[62] Xu, X. W.; Jerca, V. V.; Hoogenboom, R. Bioinspired double network hydrogels: From covalent double network hydrogels via hybrid double network hydrogels to physical double network hydrogels. *Mater. Horiz.* **2021**, *8*, 1173–1188.
[63] Wu, S. W.; Hua, M. T.; Alsaid, Y.; Du, Y. J.; Ma, Y. F.; Zhao, Y. S.; Lo, C. Y.; Wang, C. R.; Wu, D.; Yao, B. W. et al. Poly(vinyl alcohol) hydrogels with broad-range tunable mechanical properties via the hofmeister effect. *Adv. Mater.* **2021**, *33*, 2007829.
[64] Chen, J. W.; Wang, J. W.; Ji, K. Y.; Jiang, B.; Cui, X.; Sha, W.; Wang, B. J.; Dai, X. H.; Hua, Q. L.; Wan, L. Y. et al. Flexible, stretchable, and transparent InGaN/GaN multiple quantum wells/polyacrylamide hydrogel-based light emitting diodes. *Nano Res.* **2022**, *15*, 5492–5499.
[65] Zou, J.; Wu, S. Q.; Chen, J.; Lei, X. J.; Li, Q. H.; Yu, H.; Tang, S.; Ye, D. D. Highly efficient and environmentally friendly fabrication of robust, programmable, and biocompatible anisotropic, all-cellulose, wrinkle-patterned hydrogels for cell alignment. *Adv.*

Mater. **2019**, *31*, 1904762.

[66] Zeng, Z. H.; Chen, M. J.; Pei, Y. M.; Shahabadi, S. I. S.; Che, B. Y.; Wang, P. Y.; Lu, X. H. Ultralight and flexible polyurethane/silver nanowire nanocomposites with unidirectional pores for highly effective electromagnetic shielding. *ACS Appl. Mater. Interfaces* **2017**, *9*, 32211–32219.

[67] Zhou, Q. Y.; Lyu, J.; Wang, G.; Robertson, M.; Qiang, Z.; Sun, B.; Ye, C. H.; Zhu, M. F. Mechanically strong and multifunctional hybrid hydrogels with ultrahigh electrical conductivity. *Adv. Funct. Mater.* **2021**, *31*, 2104536.

[68] Yang, W. X.; Shao, B. W.; Liu, T. Y.; Zhang, Y. Y.; Huang, R.; Chen, F.; Fu, Q. Robust and mechanically and electrically self-healing hydrogel for efficient electromagnetic interference shielding. *ACS Appl. Mater. Interfaces* **2018**, *10*, 8245–8257.

[69] Zeng, Z. H.; Wang, C. X.; Siqueira, G.; Han, D. X.; Huch, A.; Abdolhosseinzadeh, S.; Heier, J.; Nüesch, F.; Zhang, C. F.; Nyström, G. Nanocellulose-MXene biomimetic aerogels with orientation-tunable electromagnetic interference shielding performance. *Adv. Sci.* **2020**, *7*, 2000979.

[70] Wei, J. J.; Zhu, C. L.; Zeng, Z. H.; Pan, F.; Wan, F. Q.; Lei, L. W.; Nyström, G.; Fu, Z. Y. Bioinspired cellulose-integrated MXene-based hydrogels for multifunctional sensing and electromagnetic interference shielding. *Interdiscip. Mater.*, in press, https://doi.org/10.1002/idm2.12026.

[71] Yu, Y. H.; Yi, P.; Xu, W. B.; Sun, X.; Deng, G.; Liu, X. F.; Shui, J. L.; Yu, R. H. Environmentally tough and stretchable MXene organohydrogel with exceptionally enhanced electromagnetic interference shielding performances. *Nano-Micro Lett.* **2022**, *14*, 77.

[72] Lu, B. Y.; Yuk, H.; Lin, S. T.; Jian, N. N.; Qu, K.; Xu, J. K.; Zhao, X. H. Pure PEDOT: PSS hydrogels. *Nat. Commun.* **2019**, *10*, 1043.

[73] Sarkar, B.; Li, X. D.; Quenneville, E.; Carignan, L. P.; Wu, K.; Cicoira, F. Lightweight and flexible conducting polymer sponges and hydrogels for electromagnetic interference shielding. *J. Mater. Chem. C* **2021**, *9*, 16558–16565.

[74] Feig, V. R.; Tran, H.; Lee, M.; Bao, Z. A. Mechanically tunable conductive interpenetrating network hydrogels that mimic the elastic moduli of biological tissue. *Nat. Commun.* **2018**, *9*, 2740.

[75] Wang, J.; Li, Q.; Li, K. C.; Sun, X.; Wang, Y. Z.; Zhuang, T. T.; Yan, J. J.; Wang, H. Ultra-high electrical conductivity in filler-free polymeric hydrogels toward thermoelectrics and electromagnetic interference shielding. *Adv. Mater.* **2022**, *34*, e2109904.

[76] Liu, J.; McKeon, L.; Garcia, J.; Pinilla, S.; Barwich, S.; Möbius, M.; Stamenov, P.; Coleman, J. N.; Nicolosi, V. Additive manufacturing of Ti_3C_2-MXene-functionalized conductive polymer hydrogels for electromagnetic-interference shielding. *Adv. Mater.* **2022**, *34*, 2106253.

[77] Chen, Z.; Chen, Y. J.; Hedenqvist, M. S.; Chen, C.; Cai, C.; Li, H.; Liu, H. Z.; Fu, J. Multifunctional conductive hydrogels and their applications as smart wearable devices. *J. Mater. Chem. B* **2021**, *9*, 2561–2583.

[78] Zhang, W.; Feng, P.; Chen, J.; Sun, Z. M.; Zhao, B. X. Electrically conductive hydrogels for flexible energy storage systems. *Prog. Polym. Sci.* **2019**, *88*, 220–240.

[79] Huang, X.; Wang, L. B.; Shen, Z. H.; Ren, J. F.; Chen, G. X.; Li, Q. F.; Zhou, Z. Super-stretchable and self-healing hydrogel with a three-dimensional silver nanowires network structure for wearable sensor and electromagnetic interference shielding. *Chem. Eng. J.* **2022**, *446*, 137136.

[80] Xiang, M.; Niu, H. W.; Qin, S.; Yang, R. M.; Lin, W.; Zhou, S. L.; Yang, Z.; Dong, S. Modification of graphene by polypyrrole and ionic liquids for dual-band electromagnetic interference shielding hydrogels. *J. Mater. Sci.* **2022**, *57*, 10983–10996.

[81] Guo, Z. Y.; Li, Y. Y.; Jin, P.; Zhang, T. T.; Zhao, Y. B.; Ai, Y. Q.; Xiu, H.; Zhang, Q.; Fu, Q. Poly(vinyl alcohol)/MXene biomimetic aerogels with tunable mechanical properties and electromagnetic interference shielding performance controlled by pore structure. *Polymer* **2021**, *230*, 124101.

[82] Wang, X. H.; Bao, S.; Hu, F. Y.; Shang, S. Y.; Chen, Y. Q.; Zhao, N.; Zhang, R.; Zhao, B.; Fan, B. B. The effect of honeycomb pore size on the electromagnetic interference shielding performance of multifunctional 3D honeycomb-like Ag/$Ti_3C_2T_x$ hybrid structures. *Ceram. Int.* **2022**, *48*, 16892–16900.

[83] Yang, X. T.; Fan, S. G.; Li, Y.; Guo, Y. Q.; Li, Y. G.; Ruan, K. P.; Zhang, S. M.; Zhang, J. L.; Kong, J.; Gu, J. W. Synchronously improved electromagnetic interference shielding and thermal conductivity for epoxy nanocomposites by constructing 3D copper nanowires/thermally annealed graphene aerogel framework. *Compos. Part A Appl. Sci. Manuf.* **2020**, *128*, 105670.

[84] Liang, C. L.; Qiu, H.; Han, Y. Y.; Gu, H. B.; Song, P.; Wang, L.; Kong, J.; Cao, D. P.; Gu, J. W. Superior electromagnetic interference shielding 3D graphene nanoplatelets/reduced graphene oxide foam/epoxy nanocomposites with high thermal conductivity. *J. Mater. Chem. C* **2019**, *7*, 2725–2733.

[85] Liang, C. B.; Qiu, H.; Song, P.; Shi, X. T.; Kong, J.; Gu, J. W. Ultra-light MXene aerogel/wood-derived porous carbon composites with wall-like "mortar/brick" structures for electromagnetic interference shielding. *Sci. Bull.* **2020**, *65*, 616–622.

[86] Yu, Z.; Dai, T. W.; Yuan, S. W.; Zou, H. W.; Liu, P. B. Electromagnetic interference shielding performance of anisotropic polyimide/graphene composite aerogels. *ACS Appl. Mater. Interfaces* **2020**, *12*, 30990–31001.

[87] Sambyal, P.; Iqbal, A.; Hong, J.; Kim, H.; Kim, M. K.; Hong, S. M.; Han, M. K.; Gogotsi, Y.; Koo, C. M. Ultralight and mechanically robust $Ti_3C_2T_x$ hybrid aerogel reinforced by carbon nanotubes for electromagnetic interference shielding. *ACS Appl. Mater. Interfaces* **2019**, *11*, 38046–38054.

[88] Fu, P. P.; Huan, X. H.; Luo, J. T.; Ren, S. J.; Jia, X. L.; Yang, X. P. Magnetically aligned Fe_3O_4 nanowires-reduced graphene oxide for gas barrier, microwave absorption, and EMI shielding. *ACS Appl. Nano Mater.* **2020**, *3*, 9340–9355.

[89] Pan, D.; Yang, G.; Abo-Dief, H. M.; Dong, J. W.; Su, F. M.; Liu, C. T.; Li, Y. F.; Xu, B. B.; Murugadoss, V.; Naik, N. et al. Vertically aligned silicon carbide nanowires/boron nitride cellulose aerogel networks enhanced thermal conductivity and electromagnetic absorbing of epoxy composites. *Nano-Micro Lett.* **2022**, *14*, 118.

[90] Zhang, Y.; Xu, M. K.; Wang, Z. G.; Zhao, T. Y.; Liu, L. X.; Zhang, H. B.; Yu, Z. Z. Strong and conductive reduced graphene oxide-MXene porous films for efficient electromagnetic interference shielding. *Nano Res.* **2022**, *15*, 4916–4924.

[91] Li, X. H.; Liu, P. F.; Li, X. F.; An, F.; Min, P.; Liao, K. N.; Yu, Z. Z. Vertically aligned, ultralight and highly compressive all-graphitized graphene aerogels for highly thermally conductive polymer composites. *Carbon* **2018**, *140*, 624–633.

[92] Li, M. M.; Han, F. Y.; Jiang, S.; Zhang, M. L.; Xu, Q. Y.; Zhu, J. H.; Ge, A. X.; Liu, L. F. Lightweight cellulose nanofibril/reduced graphene oxide aerogels with unidirectional pores for efficient electromagnetic interference shielding. *Adv. Mater. Interfaces* **2021**, *8*, 2101437.

[93] Wu, X. Y.; Han, B. Y.; Zhang, H. B.; Xie, X.; Tu, T. X.; Zhang, Y.; Dai, Y.; Yang, R.; Yu, Z. Z. Compressible, durable and conductive polydimethylsiloxane-coated MXene foams for high-performance electromagnetic interference shielding. *Chem. Eng. J.* **2020**, *381*, 122622.

[94] Chithra, A.; Wilson, P.; Vijayan, S.; Rajeev, R.; Prabhakaran, K. Carbon foams with low thermal conductivity and high EMI shielding effectiveness from sawdust. *Ind. Crops. Prod.* **2020**, *145*, 112076.

[95] Li, M. Z.; Jia, L. C.; Zhang, X. P.; Yan, D. X.; Zhang, Q. C.; Li, Z. M. Robust carbon nanotube foam for efficient electromagnetic interference shielding and microwave absorption. *J. Colloid Interf. Sci.* **2018**, *530*, 113–119.

[96] Munier, P.; Gordeyeva, K.; Bergström, L.; Fall, A. B. Directional freezing of nanocellulose dispersions aligns the rod-like particles and produces low-density and robust particle networks. *Biomacromolecules* **2016**, *17*, 1875–1881.

[97] Zhang, H. F.; Hussain, I.; Brust, M.; Butler, M. F.; Rannard, S. P.; Cooper, A. I. Aligned two-and three-dimensional structures by directional freezing of polymers and nanoparticles. *Nat. Mater.* **2005**, *4*, 787–793.

[98] Kuang, J.; Liu, L. Q.; Gao, Y.; Zhou, D.; Chen, Z.; Han, B. H.;

Zhang, Z. A hierarchically structured graphene foam and its potential as a large-scale strain-gauge sensor. *Nanoscale* **2013**, *5*, 12171–12177.

[99] Xu, Y. D.; Lin, Z. Q.; Yang, Y. Q.; Duan, H. J.; Zhao, G. Z.; Liu, Y. Q.; Hu, Y. G.; Sun, R.; Wong, C. P. Integration of efficient microwave absorption and shielding in a multistage composite foam with progressive conductivity modular design. *Mater. Horiz.* **2022**, *9*, 708–719.

[100] Zhao, B.; Bai, P. W.; Wang, S.; Ji, H. Y.; Fan, B. B.; Zhang, R.; Che, R. C. High-performance joule heating and electromagnetic shielding properties of anisotropic carbon scaffolds. *ACS Appl. Mater. Interfaces* **2021**, *13*, 29101–29112.

[101] Xiong, Z. C.; Zhu, Y. J.; Wang, Z. Y.; Chen, Y. Q.; Yu, H. P. Tree-inspired ultralong hydroxyapatite nanowires-based multifunctional aerogel with vertically aligned channels for continuous flow catalysis, water disinfection, and solar energy-driven water purification. *Adv. Funct. Mater.* **2022**, *32*, 2106978.

[102] Zeng, Z. H.; Mavrona, E.; Sacré, D.; Kummer, N.; Cao, J. M.; Mueller, L. A. E.; Hack, E.; Zolliker, P.; Nyström, G. Terahertz birefringent biomimetic aerogels based on cellulose nanofibers and conductive nanomaterials. *ACS Nano* **2021**, *15*, 7451–7462.

[103] Bian, R. J.; He, G. L.; Zhi, W. Q.; Xiang, S. L.; Wang, T. W.; Cai, D. Y. Ultralight MXene-based aerogels with high electromagnetic interference shielding performance. *J. Mater. Chem. C* **2019**, *7*, 474–478.

[104] Chen, Y. M.; Zhang, L.; Mei, C. T.; Li, Y.; Duan, G. G.; Agarwal, S.; Greiner, A.; Ma, C. X.; Jiang, S. H. Wood-inspired anisotropic cellulose nanofibril composite sponges for multifunctional applications. *ACS Appl. Mater. Interfaces* **2020**, *12*, 35513–35522.

[105] Jin, L. Y.; Wang, P.; Cao, W. J.; Song, N.; Ding, P. Isolated solid wall-assisted thermal conductive performance of three-dimensional anisotropic MXene/graphene polymeric composites. *ACS Appl. Mater. Interfaces* **2021**, *14*, 1747–1756.

[106] Li, X. H.; Li, X. F.; Liao, K. N.; Min, P.; Liu, T.; Dasari, A.; Yu, Z. Z. Thermally annealed anisotropic graphene aerogels and their electrically conductive epoxy composites with excellent electromagnetic interference shielding efficiencies. *ACS Appl. Mater. Interfaces* **2016**, *8*, 33230–33239.

[107] Tetik, H.; Orangi, J.; Yang, G.; Zhao, K. R.; Bin Mujib, S.; Singh, G.; Beidaghi, M.; Lin, D. 3D printed MXene aerogels with truly 3D macrostructure and highly engineered microstructure for enhanced electrical and electrochemical performance. *Adv. Mater.* **2022**, *34*, 2104980.

[108] Song, J. W.; Chen, C. J.; Yang, Z.; Kuang, Y. D.; Li, T.; Li, Y. J.; Huang, H.; Kierzewski, I.; Liu, B. Y.; He, S. M. et al. Highly compressible, anisotropic aerogel with aligned cellulose nanofibers. *ACS Nano* **2018**, *12*, 140–147.

[109] Yuan, Y.; Sun, X. X.; Yang, M. L.; Xu, F.; Lin, Z. S.; Zhao, X.; Ding, Y. J.; Li, J. J.; Yin, W. L.; Peng, Q. Y. et al. Stiff, thermally stable and highly anisotropic wood-derived carbon composite monoliths for electromagnetic interference shielding. *ACS Appl. Mater. Interfaces* **2017**, *9*, 21371–21381.

[110] Zhao, S.; Zhang, H. B.; Luo, J. Q.; Wang, Q. W.; Xu, B.; Hong, S.; Yu, Z. Z. Highly electrically conductive three-dimensional $Ti_3C_2T_x$ MXene/reduced graphene oxide hybrid aerogels with excellent electromagnetic interference shielding performances. *ACS Nano* **2018**, *12*, 11193–11202.

[111] Huang, S.; Wang, L.; Li, Y. C.; Liang, C. B.; Zhang, J. L. Novel $Ti_3C_2T_x$ MXene/epoxy intumescent fire-retardant coatings for ancient wooden architectures. *J. Appl. Polym. Sci.* **2021**, *138*, 50649.

[112] Gao, W. W.; Zhao, N. F.; Yu, T.; Xi, J. B.; Mao, A. R.; Yuan, M. Q.; Bai, H.; Gao, C. High-efficiency electromagnetic interference shielding realized in nacre-mimetic graphene/polymer composite with extremely low graphene loading. *Carbon* **2020**, *157*, 570–577.

[113] Song, P.; Ma, Z. L.; Qiu, H.; Ru, Y. F.; Gu, J. W. High-efficiency electromagnetic interference shielding of rGO@FeNi/epoxy composites with regular honeycomb structures. *Nano-Micro Lett.* **2022**, *14*, 51.

[114] Liu, P. B.; Wang, Y.; Zhang, G. Z.; Huang, Y.; Zhang, R. X.; Liu, X. H.; Zhang, X. F.; Che, R. C. Hierarchical engineering of double-shelled nanotubes toward hetero-interfaces induced polarization and microscale magnetic interaction. *Adv. Funct. Mater.*, in press, https://doi.org/10.1002/adfm.202202588.

[115] Li, C.; Qi, X. S.; Gong, X.; Peng, Q.; Chen, Y. L.; Xie, R.; Zhong, W. Magnetic-dielectric synergy and interfacial engineering to design yolk–shell structured CoNi@void@C and CoNi@void@C@MoS_2 nanocomposites with tunable and strong wideband microwave absorption. *Nano Res.* **2022**, *15*, 6761–6771.

[116] Liu, P. B.; Gao, S.; Zhang, G. Z.; Huang, Y.; You, W. B.; Che, R. C. Hollow engineering to Co@N-doped carbon nanocages via synergistic protecting-etching strategy for ultrahigh microwave absorption. *Adv. Funct. Mater.* **2021**, *31*, 2102812.

[117] Li, C.; Li, Z. H.; Qi, X. S.; Gong, X.; Chen, Y. L.; Peng, Q.; Deng, C. Y.; Jing, T.; Zhong, W. A generalizable strategy for constructing ultralight three-dimensional hierarchical network heterostructure as high-efficient microwave absorber. *J. Colloid Interface Sci.* **2022**, *605*, 13–22.

[118] Zeng, Z. H.; Wang, C. X.; Zhang, Y. F.; Wang, P. Y.; Shahabadi, S. I. S.; Pei, Y. M.; Chen, M. J.; Lu, X. H. Ultralight and highly elastic graphene/lignin-derived carbon nanocomposite aerogels with ultrahigh electromagnetic interference shielding performance. *ACS Appl. Mater. Interfaces* **2018**, *10*, 8205–8213.

[119] Fei, Y.; Liang, M.; Yan, L. W.; Chen, Y.; Zou, H. W. Co/C@cellulose nanofiber aerogel derived from metal-organic frameworks for highly efficient electromagnetic interference shielding. *Chem. Eng. J.* **2020**, *392*, 124815.

[120] Wang, L.; Song, P.; Lin, C. T.; Kong, J.; Gu, J. W. 3D shapeable, superior electrically conductive cellulose nanofibers/$Ti_3C_2T_x$ MXene aerogels/epoxy nanocomposites for promising EMI shielding. *Research* **2020**, *2020*, 4093732.

[121] Xu, H. X.; Zhang, G. Z.; Wang, Y.; Ning, M. Q.; Ouyang, B.; Zhao, Y.; Huang, Y.; Liu, P. B. Size-dependent oxidation-induced phase engineering for MOFs derivatives via spatial confinement strategy toward enhanced microwave absorption. *Nano-Micro Lett.* **2022**, *14*, 102.

[122] Zhang, J. J.; Qi, X. S.; Gong, X.; Peng, Q.; Chen, Y. L.; Xie, R.; Zhong, W. Microstructure optimization of core@shell structured MSe_2/$FeSe_2$@$MoSe_2$ (M = Co, Ni) flower-like multicomponent nanocomposites towards high-efficiency microwave absorption. *J. Mater. Sci. Technol.* **2022**, *128*, 59–70.